Exploring the electrical conductance of single molecules via mechanically controllable break junctions

Inauguraldissertation

zur
Erlangung der Würde eines Doktors der Philosophie
vorgelegt der
Philosophisch-Naturwissenschaftlichen Fakultät
der Universität Basel

von

Roman A. Huber
aus Liestal BL

UNI
BASEL

Basel, 2008

Genehmigt von der Philosophisch-Naturwissenschaftlichen Fakultät
auf Antrag von
Prof. Dr. C. Schönenberger
Prof. Dr. H. B. Weber
Prof. Dr. M. R. Bryce
Dr. M. Calame

Basel, den 11. Dezember 2007

                                        Prof. Dr. Hans-Peter Hauri
                                                    Dekan

The most exciting phrase to hear in science,
the one that heralds new discoveries,
is not "Eureka!" but "That's funny …"

Isaac Asimov

Contents

Preamble

In December 1947 the first transistor was invented at Bell Labs by W. Shockley, J. Bardeen, and W. Brattain and 1958 the first integrated circuit (IC) was introduced by J. Kilby at Texas instruments. Mass production became possible after the invention of the first planar transistor by J. Hoerni (1958) and the first IC available as a monolithic chip at Fairchild Corp. (1961). These two developments finally resulted in a continuous miniaturization of semiconductor devices. Since 1960 the number of transistors on an integrated circuit has doubled every two years. This trend was predicted by Gordon Moore, the co-founder of Intel Corporation, in 1965. It is generally known as "Moore's Law" [1] and still valid in 2007. Meanwhile lithography has reached feature sizes of 45 nm. The semi conductor industry expects to shrink their structures further down within the next decade. At this level, quantum effects will start to play an important role and will prevent a further miniaturization.

To extend the foreseen limits of silicon integrated circuits, new creative concepts have been proposed. These can range from quantum to biological computing, with the field of Molecular Electronics in between. The goal of Molecular Electronics is to combine electrical circuits with single or small networks of molecules, incorporating distinct electrical functions. The first proposal in this direction was made by Kuhn [2] in 1971 followed by Aviram and Ratner [3] in 1974. At that time the realization of such devices was technologically impossible. However, with the advancement of lithography devices these visions are coming within reach.

Molecules offer a variety of beneficial characteristics: They are at least an order of magnitude smaller than the features on currently existing microelectronic devices. Chemical synthesis can deliver large amounts of identical molecules. Chemists can even design and engineer attributes of molecules. Furthermore, the intrinsic characteristics of molecules can be tailored and modified by changing the physical environment (solvent, electrical potential, temperature, light). In addition, molecules can self assemble in 2D

or 3D structures. Therefore, with molecules mimicking logical components, nanometric data storage devices may be possible.

When reaching nanometer dimensions, objects become much more prone to fluctuations, an intrinsic feature in molecular junctions. Providing electrical contacts to a single molecule is already "per se" a challenging task, which has triggered a good deal of creativity among scientists. From these considerations it appears that a statistical approach will be mandatory to address and understand the properties of molecular junctions. From here on a next challenge becomes immediately clear: how to control the electronic properties of a molecular junction? A handle providing some modulation of charge transport through the molecule is essential, but conventional gating appears delicate to implement in the nanometer regime. However, molecules are interesting because they can chemically react, e.g.: form bonds or oxidize. In most cases, in order to control the reaction, this will happen in a solvent. Working in a liquid environment therefore appears to be a natural way to gain control on the molecule, either by choosing an appropriate solvent, by electrochemical gating and/or by carrying out chemical reactions *in situ*.

Beyond the fact that molecular devices may represent a cheap alternative to traditional semiconducting devices, where fabrication processes are extremely complex and costly, their advantage lies for most of it in their reactivity to the environment. While molecules are probably not suited to replace solid-state devices, they open new routes for different electronics by providing a deeper insight in the electron transfer process at the level of single molecules.

This thesis

In this thesis we use a mechanically controllable break junction technique to measure the electric transport properties of single molecules. This technique allows to control the distance between two atomic sized contacts, matching the size of a molecule. Via an implemented liquid cell we are further able to investigate molecules in a controlled liquid environment. We start with a study on "simple" test molecules, as octanedithiol or bipyridine, to obtain a better understanding on metal-molecule-metal junctions. To overcome molecular fluctuations, we introduce a robust statistical analysis of repeatedly formed molecular junctions. We then move on and compare the conductance of four different conjugated oligomers. Finally, we show the immobilization of new switchable molecules, which incorporates the previously studied conjugated molecules.

This thesis is structured as follows:

- Chapter 1 gives a brief introduction on mechanically controllable break junctions, basic theory on electron transport through single atoms as well as molecules and a quick look into data analysis by histograms.

- Chapter 2 describes the fabrication process of a break junction as well as the setup which we built to measure molecules in a liquid environment.

- In Chapter 3 we present a single molecule measurement of bipyridine and octanedithiol and on this basis a robust statistical analysis without any data selection.

- Chapter 4 shows a comparison of conductance of four conjugated oligomers at the single molecule level.

- In Chapter 5 we demonstrate the immobilization of a newly synthesized molecule with the potential of a molecular switch in the break junction.

Chapter 1

Introduction

To investigate electron transport through molecules, one first needs the appropriate contacts. In this thesis we use a mechanically controllable break junction method (MCBJ). In the first Chapter we explain the principle of this method as well as the basic theory of atomic sized contacts and molecules in between the latter.

1.1 Mechanically controllable break junction

The principle of mechanically controllable break junction (MCBJ) samples is depicted in (Fig. 1.1) and goes as follows: A metallic lead, with a free standing constriction in its middle is put on an electrically isolated, flexible substrate. By bending the substrate in a 3-point-bending mechanism a push-rod presses from the bottom and the sample is hold by two counter supports, the constriction gets stretched and is eventually broken. In the best case, this results in two mono-atomic nano electrodes which can be brought back into contact by relaxing the substrate. The gap distance d between the electrodes can now be adjusted by moving the push-rod. Assuming that the bending of the substrate is elastic, the gap size d is proportional to the push-rod movement z. The reduction factor is given by $r = z/d$ and further, the attenuation factor by

$$a = \frac{1}{r} = \frac{d}{z}.$$
(1.1)

A first implementation of this principle [4] was via a "hand made" break
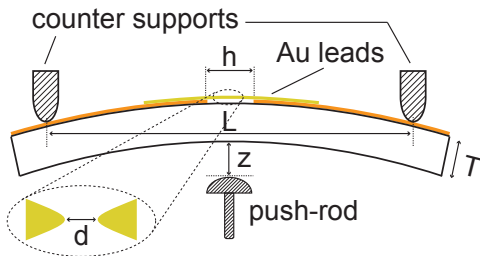
Figure 1.1: Principle of a mechanically controllable break junction. While bending the substrate the metallic constriction breaks. The distance between the resulting nano contacts can be adjusted with sub nanometric resolution by moving the push-rod.

junction. A thin metallic wire is soldered on a flexible substrate, and then notched manually under a microscope with a scalpel, reaching the free standing constriction.

A microfabricated MCBJ on silicon was first presented by Zhou *et al.* [5] and further developed on a flexible substrate by Ruitenbeek *et al.* [6]. Following this technique, we built our own MCBJ setup and samples which are explained in detail in Chapter 2. The big advantage of the microfabricated break junction technique is, on the one hand, the far higher attenuation factor (at least two orders of magnitude) and therefore the higher stability of the junction. The higher attenuation factor is due to the smaller under etched part h of the microfrabricated sample. On the other hand, the lower leakage current in solvents in consequence of the smaller contacts: The leakage current is due to the ion movement in solution, driven by a potential difference. This leakage current is proportional to the surface area of the contacts. To reduce the leakage current it is therefore desired to have very small contacts or to expose only little of the contact area to the liquid, e.g. by covering the contacts with an insulating layer.

To calculate the theoretical value of the attenuation factor a_g, one has to distinguish between several cases [7], for instance whether the flexible substrate has supported or fixed ends or whether the curvature mimics a circle. This distinction of the approach already leads to a variation of the reduction factor by a factor of 3. For the ideal case of an elastically homogeneous bending beam with supported ends, the attenuation factor is given by

$$a_g = \frac{6Th}{L^2} \tag{1.2}$$

Based on our geometry with the thickness of the substrate $T = 0.3\ mm$, the distance between the counter supports $L = 20\ mm$ and the length of the free standing bridge $h \approx 0.5\ \mu$m we get $a_g \approx 2 \cdot 10^{-6}$. In practice, the plastic deformation of the sample results in an increase of a_g by approximately one order of magnitude [8]. The typical materials we used for the substrate are phosphor bronze and spring steel. Performing an experimental calibration [9; 10] of a we get $a = 5 \cdot 10^{-5}$ for phosphor bronze and $a_g = 1.6 - 4 \cdot 10^{-5}$ for spring steel substrate samples. This experimental calibration is performed by measuring the variation of the tunneling current with the gap size in vacuum, after the breakage of the junction. The attenuation factor is then derived by using the established value for the workfunction of gold (3.5-5.0 eV) [11].

With the mechanically controllable break junction technique we have a method to fabricate metal contacts of atomic size. When scaling down to atomic-sized conductors, simple concepts like Ohm's law ar not longer applicable. In the next Section we will therefore discuss the basic theory for small conductors.

1.2 Conductance of metal point contacts

The conductance of a macroscopic conductor is characterized by Ohm's law. It reveals the conductance directly proportional to the transverse area A and inverse proportional to the length L. With σ the conductivity of the sample it is given by:

$$G = \frac{\sigma A}{L} \tag{1.3}$$

Electron transport properties through small conductors were first described by Maxwell [12]. Classically, we can model the point-contact as a constriction in the material. Hence, Maxwell considered a constriction of hyperbolic geometry. By using oblate spheroidal coordinates (ξ, η, φ) it is therefore possible to obtain an analytic solution. The Maxwell conductance is then given by:

$$G_M = 2a\sigma(1 - sin\eta_0). \tag{1.4}$$

Where σ is the conductivity of the material and $2a$ the distance between the foci. In the limiting case of $\eta_0 = 0$ the contact is reduced to a circle of radius a, and the conductance is $G_M = 2a\sigma$

When scaling down to mesoscopic systems one has to consider different length scales, leading to different scattering mechanisms.

1. Electron transport in metals occurs via electrons with an energy close to the Fermi energy E_F. Electrons are associated with the *de Broglie wavelength* λ_F. When the size of the conductor gets comparable with λ_F, the wave nature of the electrons becomes essential to understand the transport process.

2. The *elastic mean free path l*, which measures the distance between elastic collisions with static impurities. The regime $l \ll L$ is called diffusive, whereas at $l > L$ we reach the ballistic regime (Fig. 1.2). In the diffusive regime incident electrons are scattered at impurities. The resulting electron motion can be described as a random walk of step size l between the impurities. In contrast to that, in the ballistic regime, the electron momentum is only limited by scattering with the boundaries of the sample.

3. The *phase coherence length L_φ*, which measures the distance over which quantum coherence is preserved.
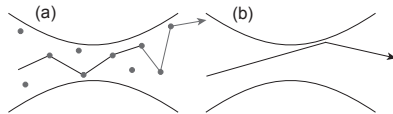
Figure 1.2: Schematic illustration of (a) a diffusive and (b) a ballistic conductor.

If we further reduce the size of the conductor until it gets much smaller than the dimension of the mean free path l, the electrons will pass through ballistically. Due to a large potential gradient near the contact, the electrons will be accelerated within a short distance. It was Sharvin [13], who first considered the conductance through this type of junctions. By using a semiclassically approximation he derived the conductance to

$$G_S = \frac{2e^2}{h}(\frac{k_F a}{2})^2 \,. \tag{1.5}$$

where k_F is the Fermi wave vector, h Planck's constant and a the contact radius. This model is independent of the conductivity σ and the mean free path l. Therefore quantum mechanics only enters through the Fermi statistics.

By further reducing the conductor, the wave nature of the electrons start to play a role also. A scattering approach is used to describe the conductance

through metal point contacts connected to macroscopic electrodes [14]. The idea of the scattering approach is to relate the transport properties of a conductor to the transmission and reflection probabilities for carriers incident on the sample.
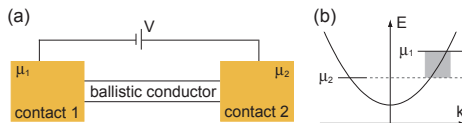
Figure 1.3: (a) Schematic illustration of a one dimensional conductor. (b) Dispersion relation for electrons in the conduction band of a metal.

For simplicity we first consider a metallic, one dimensional conductor, in contact with two large contacts having chemical potentials μ_1 and μ_2 (Fig. 1.3(a)). If we assume μ_1 greater than μ_2, electrons are flowing from the first reservoir to the second. The resulting current is given by:

$$I = \frac{2e}{h} \int_{\mu_2}^{\mu_1} dE = \frac{2e}{h}(\mu_1 - \mu_2). \tag{1.6}$$

The difference in chemical potential remains by applying a bias voltage V $= (\mu_1 - \mu_2)/e$. By definition the conductance is G=I/V and we get:

$$G_0 = \frac{2e^2}{h} = 77.5\,\mu S. \tag{1.7}$$

This demonstrates that a one dimensional conductor between two electrodes has a finite resistance, given by the universal quantity $1/G_0 = h/2e^2 \approx 12.9 k\Omega$. This is an important difference with respect to macroscopic conductors, where one expects to have zero resistance for the perfect conducting case.

We now consider a conductor connected to two large contacts by two leads [14] as shown in Fig. 1.4. The contacts have the chemical potentials μ_1 and μ_2. The leads are assumed to be ballistic conductors each having M transverse modes. T is the average probability that an electron injected in lead 1 will transmit to lead 2. In this case, the conductance is equal to

$$G = \frac{2e^2}{h}TM \tag{1.8}$$

With e the electron mass, M the number of transverse modes of a ballistic

conductor and $0 < T < 1$ the average transmission probability. This formula is know as the Landauer Formula [15; 16].
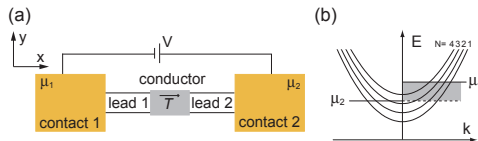
Figure 1.4: (a) A conductor having a transmission probability of T is connected to two large contacts through two leads. (b) Dispersion relations for the different transverse modes (4) in the narrow conductor. For reflectionless contacts, the quasi-Fermi level for the +k states is μ_1 while that for the -k states is μ_2.

1.3 Breaking process of a break junction

After discussing the basic electron transport theory of atomic sized conductors, we will now describe a typical breaking curve of a Au break junction. This breaking curve will then be compared to the atomic formation of the Au contacts.

In a break junction experiment the junction is repeatedly opened and closed while the conductance is recorded. Fig. 1.5 shows the typical breaking process of break junction in a liquid environment. Although the illustrated curve is recorded in liquid, the behavior is similar as in vacuum. First the contacts of the break junction are fully closed showing a conductance well above G_0. It has been proven [17] that in atomic gold contacts each gold atom contributes with a conduction channel (transverse mode). Hence, during the breaking process, the plateaus observed at n multiples of G_0 are attributed to n gold atoms in parallel in the narrowest part of the junction. Increasing the distance z will lead to only a few atoms in contact, creating plateaus in the high conductance regime (Fig. 1.3(a)). The Au-bridge gets thinner (1, 2) until a rather stable single-atom contact is established (1). After breaking open, the Au contacts retract, leading to a fast drop in G (3 to 4). In the following, we will also use the term "junction" for such a broken Au bridge. The atomic movement of the contacts stabilizes between 10^{-2} and 10^{-3} G_0 (depending on the sample) after which exponential decay is observed (line in Fig. 1.5(b)). This exponential decay with distance is due to the tunneling current between the contacts the only feature present (4 to 5). The regime below G_0 we will further call the "tunneling regime".
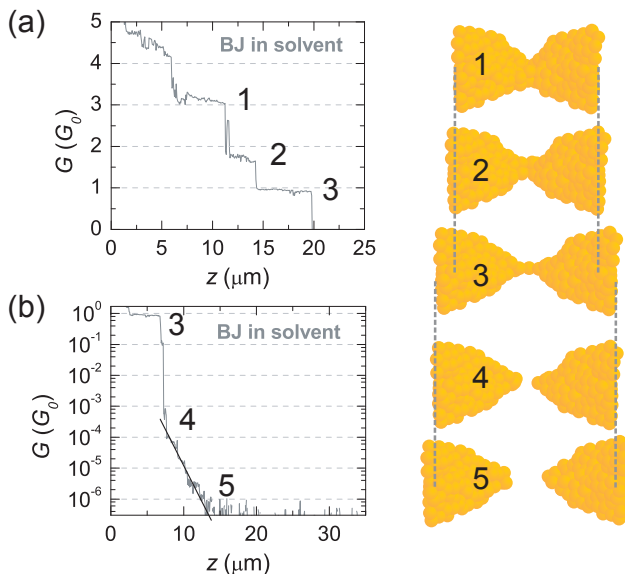
Figure 1.5: Breaking process of a break junction in liquid environment without molecules present. (a) shows the conductance curve in the high current regime and (b) in the tunneling regime.

1.4   Conductance histograms - two different representations

To analyze all the measured single conductance curves one needs to perform a statistical analysis. Due to rearrangements of the atomic contacts none of the single curves is similar to the previous ones. It's therefore a habit in the field of metallic atomic junctions and molecular electronics to construct histograms of a large bunch of single conductance curves. This analysis has first been implemented in atomic junctions [18; 19; 20], and has subsequently been used in metal-molecule junctions [21; 22; 23]. We will explain two different ways of histogram formation at the example of a measurement in a solvent. The standard way of calculating a histogram is shown in Fig. 1.6(a). By using a constant conductance bin size, all the points of the G vs. z curves are used to build the histogram. This histogram gives the probability to measure a conductance value. In Fig. 1.6(b) we show a histogram with 3 peaks, at 1, 2 and 3 G_0. For Au it has been proven this corresponds to one,

Linear Scale Histograms
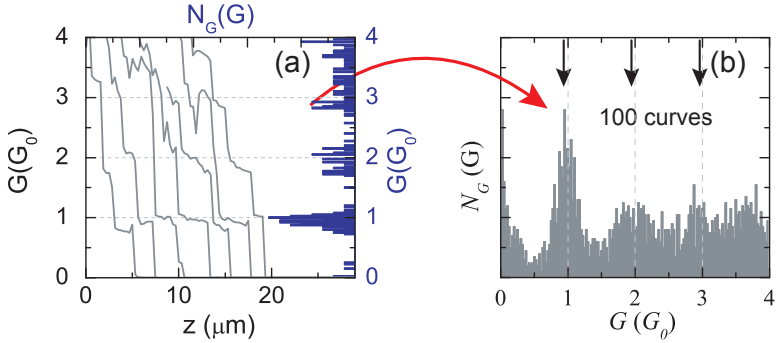
Log Scale Histograms
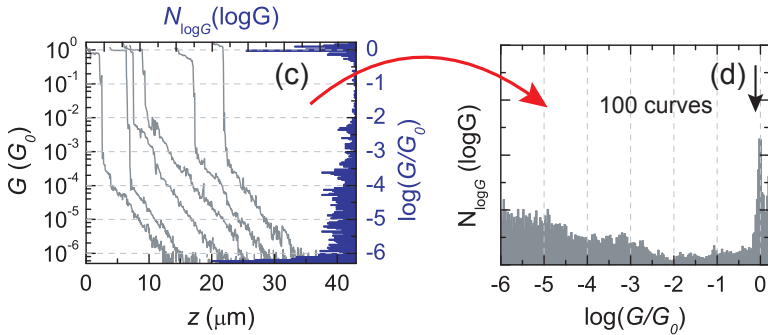
Figure 1.6: Two different styles of histograms. Whereas in (a) the linear scale is limited to a defined area of the measurement, the histogram in log-scale (b) can give a broad overview over several magnitudes. The bin sizes are 0.02 G_0 in (a) and 0.03 G_0 in (b)

two and three Au atoms in contact.

We further introduce a very nice and convincing way of histogram formation. As we show in Fig. 1.6(c) all the single curves are transformed to a *logarithmic scale* first. This gives an overview over several orders of magnitude of the curve and it enhances plateau features. The histogram is then calculated using a *constant* bin size. It shows an excellent overview between 10^{-6} G_0 and several G_0 (Fig. 1.6(d)). We like to point out the clear

peak at 1 G_0 that is caused by the mono atomic gold contact. Below 1 G_0 emerges very well the effect described in chapter 1.3. The fast retraction of gold contacts is described by a low number of counts between 10^{-3} and 1 G_0. The stabilization of the contacts is recorded by a higher number of constant counts and is therefore describing an exponential decay behavior due to tunneling between the contacts.

For a detailed analysis of the transformation between log- and linear histograms see Appendix C.

1.5 Brief history - break junction and atomic contacts

The start in the field of atomic contacts was set shortly after the invention of the scanning tunneling microscope (STM) by Binnig and Rohrer in 1981 [24]. Gimzewski and Möller were the first to specifically measure the conductance in atomic-sized contacts with an STM in 1986 [11]. The concept of a "mechanically controllable break junction" was first introduced in 1985 by Moreland and Ekin [4] for the study of the tunneling characteristics of superconductors. This technique was further extended by Muller and Van Ruitenbeek [6; 25; 26] to obtain clean and stable adjustable junctions for the study of electronic transport processes in atomic-size metallic wires. Muller *et al.* showed first results for Nb and Pt contacts, with steps in the conductance vs. displacement curves. This effect was explained by the atomic structural rearrangement mechanism in the constriction. In the following years, further experiments using different methods with atomic sized contacts were performed [18; 27; 28; 29]. During some years there was an exciting discussion about the origin of these steps. In 1996 Rubio *et al.* [30] combined a conductance and force measurement showing that steps in conductance are associated with distinct jumps in the force which gives convincing proof for the atomic rearrangements at the conductance steps. The breakthrough in the understanding of conductance at the atomic scale followed in 1997. Scheer *et al.* [17] published a study in which they allowed more than one independent conductance channel (in contrast to only one before), with transmission probabilities $\tau_n < 1$, to fit their I-V curves of superconducting single-atom contacts. This interpretation was further supported by tight binding calculations of Cuevas *et al.* [31]. To that effect the number of conductance channels is determined by the number of valence orbitals of the atom. This view was further confirmed in continuative work for various superconductors [32].

First experiments with molecules in atomic junctions were performed after 1995 in STM setups [33; 34; 35; 36]. A short time afterwards, in 1997 a mechanically controllable break junction (MCBJ) was first used by Reed *et*

al. [37] to measure the electrical conductance of molecules. This approach offered statically stable contacts and restricted the number of active molecules to as few as one. Further it convinces by its relatively simple fabrication of clean metallic atomic sized contacts with tunable gap size. These advantages led to a wide use of the MCBJ in molecular electronics. The great variability to implement this method in setups is outstanding. Experiments in liquid [10; 38; 37], vacuum [39; 40], at low temperature [22; 41; 42; 43; 44; 45; 46], argon atmosphere [47] or in combination with a UV light source [48] or a raman spectrometer [49] have been reported.

1.6 Molecular conductance

With the mechanically controllable break junction we have a tool to fabricate atomic contacts. As discussed above, its behavior is widely analyzed and understood. It is now the goal to use the break junction technique as a tool to contact molecules and measure their electrical conductance.

What is the conductance of a molecule and how can we influence it? As atomic contacts, a single molecule is also an object of a few angstroms, and conduction through it has to be also understood as a quantum process. For a molecule linked with two metallic electrodes two attributes are relevant. First the main part of the molecule itself, which can be synthesized by chemists in different ways. They can create the molecule insulating, conducting or even with distinct functionalities. The second attribute is the form of the contact between the molecule and the electrodes. Indeed it needs to be strong enough to allow a current flow, but also weak enough to keep the intrinsic features of the molecule.
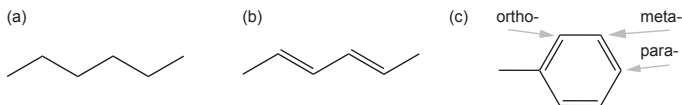
Figure 1.7: (a) Schematics of an alkane (not conjugated) and (b) of a polyene (conjugated). (c) On a benzene ring, three different positions of the anchoring group are possible: ortho-, meta- and para-position.

Often-used molecules in molecular electronics are the so called molecular wires. These are simple conjugated or non-conjugated (Fig. 1.7(a)) organic molecules. A chemically conjugated system is a system of atoms covalently bonded with alternating single and multiple bonds in an organic molecule

(Fig. 1.7(b)). It results in an overlap of all the adjacent parallel aligned p-orbitals and further overlapping π-orbitals leading to fully delocalized electrons (Fig. 1.8).
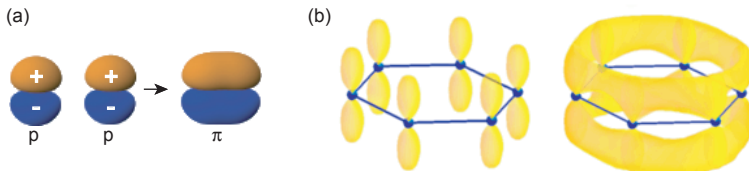
Figure 1.8: (a) Two parallel overlapping p-orbitals result in a π-orbital. (b) shows the lowest energy π molecular orbital of benzene, which is constructed from a superposition of p_z-orbitals centered on each of the six carbon atoms [50].

In an organic molecule the electron transfer passes through the frontier orbitals being closest to the fermi level of the electrodes. Therefore conjugated molecules should enhance the transport of electrons, whereas the non-conjugated molecules are mainly insulators.

In molecules with several subunits (e.g. in aromatic rings), the delocalization of the electrons depends also very much on the twist angle between the subunits. Due to the twist angle the overlap of the electronic orbitals gets weaker which results in a lower electron transport [51].

Another major influence on the conduction along the molecule has the relative position of the linker group (Fig. 1.7(c)). While ortho- and para-position keep the conjugation and allow good conduction, the meta-position gives two consecutive single bonds, destroying the conjugation and decreasing the conduction.

1.6.1 Qualitative picture

To describe the electron transfer through a metal-molecule-metal system, one has to consider the energy level diagram (Fig. 1.9(a)). The metal leads are described by a continuum of energy levels, whereas the molecule has discrete levels (molecular orbitals). The HOMO level is the highest occupied molecular orbital and therefore the last filled level. The LUMO is the lowest unoccupied molecular orbital and therefore the first empty level. Electrons can flow when one level is close to the Fermi level (E_F). Usually this is not the case, since the HOMO-LUMO gap is typically few eV. Nonetheless, it is possible to change the energy level of the leads with respect to the molecular levels by applying a bias voltage V (Fig. 1.9(b)). The lead levels
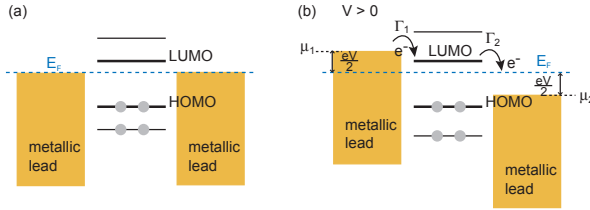
Figure 1.9: (a) Schematic energy level diagram of a metal-molecule-metal structure.

move away from the Fermi level and open an energy range of eV in which electron transfer becomes possible. In case of a bias voltage V, the left lead level moves up by $eV/2$ whereas the right moves down by $eV/2$. Assuming E_F is closer to the HOMO level at the start, the conduction takes place through the HOMO level and the LUMO will play no role. If E_F is closer to the LUMO the conduction takes place through the LUMO and the HOMO plays no role. Only the energy levels in the opened energy range allow the transport of electrons.

1.6.2 Discrete level model

A simple model [52] can be introduced by considering only one discrete molecular energy level ϵ being closest to the Fermi energy E_F. The current through the level can then be derived sequentially. The numbers of electrons occupying the level would be given by $N_1 = 2f(\epsilon, \mu_1)$ if the level were in equilibrium with the left contact and by $N_2 = 2f(\epsilon, \mu_2)$ if the level were in equilibrium with the right contact. The factor 2 comes from the spin degeneracy and $f(\epsilon, \mu)$ is the Fermi-Dirac function. In non equilibrium the number N, of electrons in the level will be somewhere in between N_1 and N_2. We can write the resulting current from the left contact to the molecule:

$$I_1 = \frac{e\Gamma_1}{\hbar}(N_1 - N) \tag{1.9}$$

and from the molecule to the right contact as:

$$I_2 = \frac{e\Gamma_2}{\hbar}(N - N_2) \tag{1.10}$$

Γ_1 and Γ_2 denote the coupling between the left and the right contact and the level. In equilibrium, I_L must be equal to I_R so that

$$N = \frac{N_1\Gamma_1 + N_2\Gamma_2}{\Gamma_1 + \Gamma_2} \tag{1.11}$$

and finally we get the net current:

$$I = I_1 = I_2 = \frac{2e}{\hbar}\frac{\Gamma_1\Gamma_2}{\Gamma_1 + \Gamma_2}[f(\epsilon, \mu_1) - f(\epsilon, \mu_2)] \tag{1.12}$$

Knowing the energy level ϵ, the coupling factors Γ_1, Γ_2 and the electrochemical potentials μ_1, μ_2 of the two contacts we can calculate the current I from eq. 1.12.

1.6.3 Model with broadening of molecular energy levels

If the molecule is strongly coupled to the metallic contacts [52], the molecular orbitals and the electronic states of the leads do overlap. This leads to a hybridization of the electronic states, and therefore a common delocalized electronic wave function extending over the whole junction. In consequence the density of states $D(E)$ (the probability of having an electron state with energy E) can not be described anymore by a Dirac delta at energy ϵ. It broadens, and is better represented by a Lorentzian density of states:

$$D(E) = \frac{1}{2\pi}\frac{\Gamma}{(E - \epsilon)^2 + (\Gamma/2)^2} \tag{1.13}$$

Including this in eq. 1.12 and integrating over the energy we finally obtain the current:

$$I = \frac{2e}{\hbar}\int_{-\infty}^{\infty} dE\, D(E)\frac{\Gamma_1\Gamma_2}{\Gamma_1 + \Gamma_2}[f(\epsilon, \mu_1) - f(\epsilon, \mu_2)] \tag{1.14}$$

The discrete level model and the model with broadening of molecular energy levels is illustrated in Fig. 1.10.
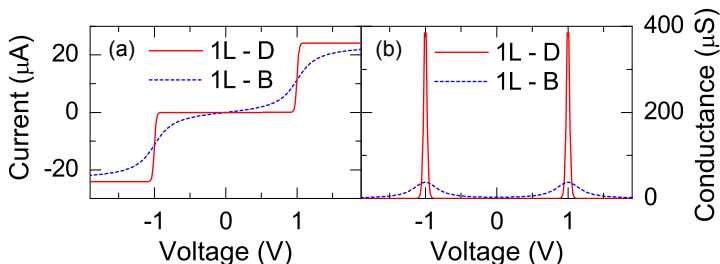
Figure 1.10: (a) Current-voltage diagram. The red curve illustrates a model for a molecule with a single energy level. The energy level is discrete, regardless with the coupling of the contacts. For the blue dashed curve, the energy level is broadened according to the coupling with the contacts. Temperature $T = 77K$, $\Gamma_1 = \Gamma_2 = 0.1\ eV$, $E_F = -5\ eV$, $E_{level} = -5.5\ eV$. (b) The corresponding conductance-voltage diagram. Simulations were performed by MolCToy on http://nanohub.org.

1.6.4 Tunneling model

As described in Section 1.6.1 conduction is possible if the molecular levels lie in the energy range (between μ_1 and μ_2, Fig. 1.9) in which electron transfer is possible. If this is not the case, we have electron tunneling from one contact to the other, assisted by the broadening of the molecular levels, which determines the barrier height ϕ.

If we look at a molecule as a distinct media between two metallic contacts, we describe the conduction by a tunneling process through a square potential-barrier (with height Φ and width d). The transmission through the barrier is given by:

$$T \sim e^{\frac{-2d}{\hbar}\sqrt{2\phi m}} \tag{1.15}$$

Using the Landauer Formula (eq. 1.8) we can estimate the conductance of the metal-molecule-metal system as:

$$G \sim G_0 e^{\frac{-2d}{\hbar}\sqrt{2\phi m}} \tag{1.16}$$

where m is the electron mass, d the length of the molecule between the metallic leads and ϕ the barrier height. Here we can further introduce the tunneling decay constant $\beta = \frac{-2}{\hbar}\sqrt{2\phi m}$. The smallest values for β are found in highly conjugated organic molecules for which β is in the range 0.2-0.6

Å^{-1} [53; 54; 55; 56; 57]. In contrast, for vacuum a β-value of ~ 2.0 Å^{-1} is found [58].

The exponential dependance of eq. 1.16 was first applied to describe transport through molecules by Mc. Connel [59]. In this context, electron transfer is also known as superexchange [60; 61; 62].

1.7 How to act on molecules

If it is possible to contact single molecules and measure the electrical conductance, it is a further goal to interact on electrical functionalities of the molecules. To interact in situ with a metal-molecule-metal junction during a measurement exist several methods which we report here briefly and which are illustrated in Fig. 1.11.

- Method (a) uses an electrostatic back gate. This method is used in the semiconductor industry for field effect transistors (FET). In a FET, the electron flow between the source and the drain is accessed by the back gate. This method was also adopted in molecular electronics. Usually the electrodes are placed on a several nm thick SiO_2 film on top of a degenerately doped silicon wafer. For example Champagne *et al.* [63] combined a MCBJ with this method of gate electrode. Further molecular measurements with a back gate have been done by Kubatkin *et al.* [64] who measured a single organic molecule with access to several redox states or Jo *et al.* [65] who measured devices incorporating magnetic molecules.

- Method (b) includes an electrochemical gate. A gate electrode is dipped into an electrolyte in which the molecules are dissolved. By applying a potential U_{gate} at the gate electrode, the counter ions in the electrolyte move towards the gate electrode. Therefore the potential of the gate is applied to the molecules through the electrolyte.

  For a well controlled electrochemical cell, three electrodes are dipped into the electrolyte: A working electrode, a reference electrode and a counter electrode. A potentiostat is used to control the potential between the working electrode and the reference electrode. The counter electrode is used to keep the working electrode potential at a constant value with respect to the reference electrode. This method is especially used in STM experiments by the groups of S. M. Lindsay [66], N. G. Tao [67] and Th. Wandlowski [68; 69].

- In method (c) the interaction is performed by incident light. Light is also a good medium to address molecules: it can be used in different

environments, with different wavelengths and has short response times. This method was also implemented in a MCBJ [48] on photochromic active molecules [70; 71; 72]. Further experiments have been done with a STM and STM Break Junction [73; 74] or gold nanoparticles [75].

- In method (d) an analyte is used that reacts with the molecule. The latter also opens the possibility of new sensing devices [76].
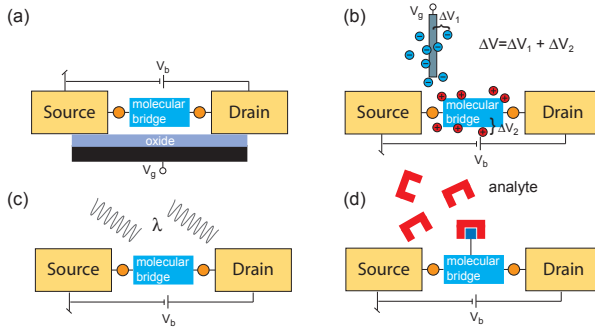
Figure 1.11: Different ways of acting on a molecule: (a) by using a back gate, (b) by using a gate electrode in a liquid environment, (c) by a light triggered photo reaction and (d) by adding an analyte that reacts with the molecule.

Chapter 2

Fabrication and experimental setup

The fabrication of the break junction samples as well as the experimental setup evolved during the time of this PhD work. On the one hand, this was necessary to decrease the fabrication time and increase the yield of the working samples. On the other hand, the setup had to fulfill more specialized and extended duties. In this part of the thesis, I will describe the standard fabrication process of a break junction sample, used machines and utilities, as well as the achieved improvements in the last years.

2.1 Sample fabrication

2.1.1 Substrate preparation

To fabricate a break junction sample, we need a flexible and electrically isolated substrate. Usually, metals covered by polyimide are used. In first experiments a 0.3 mm thick phosphore bronze substrate served as a substrate. This substrate gets easily plastically deformed and is therefore not ideal. Such deformations may influence the measurements and lead to unreproducible measurements. Hence the basic substrate was changed from phosphore bronze to spring steel. Spring steel was chosen because of its higher tensile strength compared to the phosphore bronze sheet. To isolate the substrate, a multi layer of polyimide (Pyralin PI2610 HD Microsystem) was spun on the unpolished substrate. Due to the fluid behavior of the polyimide these layers coat the rough surface and ensure the flatness of the substrate even without polishing.

The used process of coating the substrate with polyimide is as follows:

First a 6.5 x 6.5 cm piece of spring steel is cleaned in an acetone and iso-propanol bath at ultrasonic agitation. Then 3 to 4 layers of polyimide are spun at 8000 rpm for 40s on top of the metallic substrate. After each layer the substrate is baked in the oven at $200°$C for 40 minutes. Finally, the substrate is annealed for one hour at $390°$C at 10^{-5}mbar. Since spring steel is much harder compared to phosphor bronze it is very difficult to cut it with a blade without damaging it. Therefore the polyimide coated pieces were sent to a laser cutting company (Digipack AG, CH-8623 Wetzikon) to cut the 23.8 x 0.9 mm samples.
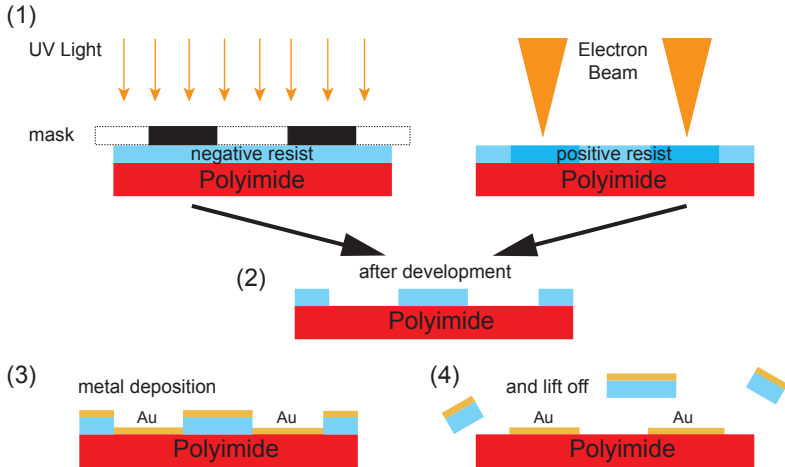
2.1.2 Lithography, metal deposition and plasma etching

A process of lithography and metal deposition was performed to pattern the gold paths on the flexible substrates. Two fabrication processes were used during the work of this PhD. In the beginning we used two lithography steps: First, optical lithography for the larger parts of the structure such as contact pads and leads; Second, electron beam (e-beam) lithography for the small junction part. These steps, including two subsequent metal depositions, are very time consuming. Furthermore it may lead to mismatches in the overlap of the two lithography steps. To reduce the fabrication time and to increase the yield of working samples, the process was optimized using only e-beam.

In lithographic processes two different types of resists can be used: a positive or a negative resist (Fig. 2.1 (1.)). In both cases first the resist is spun on a substrate and polymerized by baking on a hot plate or in the oven. By exposure of the negative resist, the illuminated part gets further polymerized and the unexposed area can be dissolved. The positive resist works the other way round and the exposed area is dissolved during development. Usually negative resists are used for optical lithography and positive resists for e-beam lithography.

Optical lithography

In optical lithography, light passes an optical mask which consists of a metal structure on glass and illuminates the substrate. The substrate is spin-coated (4000 rpm, 40s) with a negative photo resist (ma-N-415, Micro Resist Technology, Germany) followed by baking at $90°$C for 90s. An optical lithography machine (SUSS MJB3, Karl Süss KG -GmbH & Co.) with a Hg lamp is used for the exposure. The exposure time is 25 - 30 s. The sample is then developed in ma-D 332S for $\sim$ 60 s and finally rinsed in water. The size of the UV structure is limited by the wavelength of the used light. In case of the Hg lamp 365 nm. In reality, the theoretical value of our UV machine

Figure 2.1: (1) Lithography step: use of positive and negative lithography resists. (2) Development step. (3) Metal deposition and (4) The lift off step.

is reduced by backscattered light (proximity effect) so that we expect the smallest possible structures at $\sim$ 1 - 2 μm.

Electron beam lithography

Electron beam lithography (e-beam) uses an electron beam to pattern a structure on a surface. The resolution is given by the beam width (order of nanometers) and the proximity effect (backscattered electrons). It is therefore possible to make features of $\sim$ 20 - 50 nm. The structure is designed on the computer and then transferred to the e-beam machine. As e-beam resist serves a positive resist (PMMA 950 K, Allresist GmbH) diluted with additional chlorbenzene to decrease the final layer thickness ($\sim$ 600 nm), spin coated on the substrate (4000 rpm, 40s) and baked at 175°C for 30 minutes. After exposure with the e-beam, the development of the structure is done in a solution of MIBK (4-methyl-2-pentanone) and isopropanol at a ratio 1:3 for 45 seconds. The sample is then rinsed in isopropanol to stop the development (Fig. 2.1 (1) and (2)).

For the process of the e-beam lithography we first used a JEOL JSM-

IC 848 scanning electron microscope (SEM) and later a LEO SUPRA 35 SEM. The pattern design and the stage is controlled with the software Elphy Quantum from Raith GmbH. LEO offers automated control of the beam magnification and the stage movement and makes it therefore possible to write the whole break junction structure automatically in one run. The focusing of the electron beam on the substrate is hindered by the insulating polyimide layer. A small silver dot near the exposure area is therefore very helpful.

Metal deposition

After the lithography steps we have a pattern for the metal deposition on the sample surface. The sample is mounted on a tiltable sample holder in a vacuum chamber (PLS 500, Balzers-Pfeiffer GmbH) and pumped to $\sim 10^{-6}$ mbar. In addition the sample holder can be cooled to avoid that the structure's resist borders will smear out when heated by the metal. Further, it improves adhesion and density of the evaporated metal. The metal is thermally evaporated by an electron gun while the thickness of the film is controlled by a calibrated oscillating quartz crystal. The break junction consists of two layers: First, a 10 nm titanium layer is evaporated as adhesion layer under an angle of $\sim 50°$. The tilted angle ensures no titanium is located in the final bridge (Fig. 2.2(a)) while it is deposited on the broader leads. Second, 60 nm Au is evaporated perpendicular to the sample (Fig. 2.2(b)). After evaporation the sample is immersed in acetone to perform the liftoff. The final result is shown in Fig. 2.3(a). The underlaying Ti layer is still visible in the final structure and is highlighted by the white dotted line.
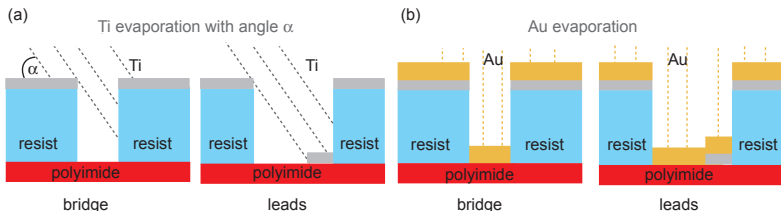

Figure 2.2: (a) First the Ti layer is evaporated under an angle of $\sim 50°$. Therefore no titanium is located in the final bridge, but it is deposited on the broader leads. (b) The Au layer is evaporated perpendicular to the sample.

Plasma etching

To finalize the break junction sample we need to obtain the free standing central metal bridge. Therefore the polyimide is dry etched with a Reactive Ion Etching (RIE) machine (PlasmaLab 80 plus, Oxford). During the etching process the contact pads are protected by a glass cover. The rest of the surface is slowly etched which results in an under etching of the narrowest part of the structure (Fig. 2.3(a)).

The etching is performed during $\sim$ 3 minutes at a flow of 2% CHF_3 and 32% oxygen at pressure of 0.1 torr and power of 100 W.
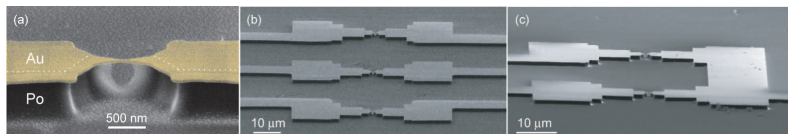
Figure 2.3: Three SEM images of break junction samples. (a) The final underetched break junction bridge. The white dotted lines mark the shadow of the Ti layer. (b) The version with 3 junctions each containing 2 contacts and (c) the time saving version with only 2 junctions and overall 3 contacts.

2.1.3 Sample optimization and time shortening

On each substrate, several break-junction structures were patterned in parallel. This was chosen to increase the yield of working samples. In the beginning, we patterned three of these structures independent of each other on one sample (Fig. 2.3(b)). Later the number was reduced to two structures sharing one contact pad (Fig. 2.3(c)). This was done to save time during the one step e-beam process. Further the third structure was found to be unnecessary. Due to the e-beam exposure of the sample in one step, only a single metal deposition step is needed. Additional time was saved by using larger sample holders (space for 10 samples) for the metal deposition as well as in the e-beam machine, allowing to produce a larger number of samples at a time.

After the optimization of the sample fabrication we are now able to produce 1 sample in $\sim$ 45 minutes (in assumption the substrates are ready). The yield of working samples is $\sim$ 90%. In comparison with the process three years ago, this is 5 times faster with an almost doubled yield of working samples.

2.2 The setup

The setup we use to operate our break junction samples consists of an apparatus to mount and bend the samples, the liquid cells for measurements in solvents and with molecules, an autoranging low-noise I to V-converter, a pre resistor to limit the maximum short current and a data acquisition board connected to a computer to record the data (Fig. 2.4). These parts are explained in detail in the following pages.
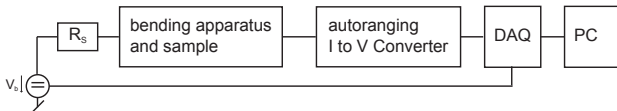
Figure 2.4: The basic circuit of the break junction measuring setup.

2.2.1 The bending apparatus

To operate a break junction sample you need a setup to bend the sample (Fig. 2.5). The sample is then mounted in this mechanical bending setup [10]: two counter supports hold the sample on the sides, while a push-rod is pressing in the center from below (z movement), bending the substrate. The distance between the two counter supports is 20 mm. The vertical displacement is driven by a stepper motor (Phythron GLD). A coupling gear, consisting of a planetary gear (reduction 1:4) and a worm gear (reduction 1:50), permits movements up to a few millimeters. One full turn of the worm gear (=50 motor turns) moves the push-rod 1 mm in vertical direction. The motor does 200 steps for one turn, each step divided electronically into 8 substeps. Therefore one step corresponds to a movement of 25 nm and one substep to 3.125 nm. The motor is controlled by a PC and the speed can be adjusted between 500 and 9999 substeps per second (1.56 - 31.2 $\mu m/s$). The high reduction factor leads to a very small sample surface elongation. To fully open/close the break junction a vertical displacement of 10-20 cycles ($\sim$ 200-400 μm) is needed. Piezo actuators fitting our setup are not able to perform such long distances (typically max. $\sim$ 100 μm) and therefore no piezo element is used in our setup.
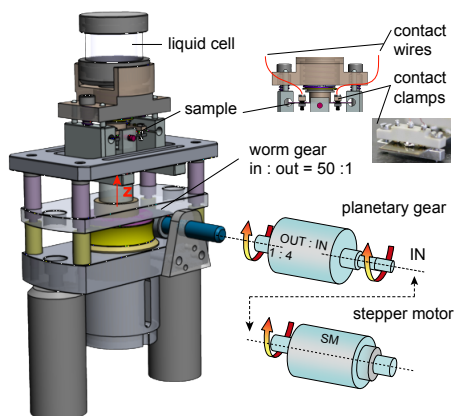
**Figure 2.5:** The bending apparatus of the break junction measurement setup.

2.2.2 Contact to the sample

The contacts to the sample need to be stable during the whole measurement. Although spring loaded contacts are a very elegant and simple way to contact the sample, it turned out to have some disadvantages. Due to the up and down movement of the sample during the measurement the spring loaded contacts slide horizontally on the contact pads and scratch the surface. Therefore a new method of contacting the samples was introduced. The contacts were fixed to the pads with a clamp and an indium layer is placed in between to ensure a proper electrical contact (photo in Fig. 2.5). In this way no movement of the contacts is possible.

2.2.3 The liquid cells

To measure in liquid environment two different liquid cells were integrated into the setup. Both cells consists of a viton tube on top of the break junction sample. The first cell [10] includes an inlet and an outlet port (Teflon tubes) allowing the exchange of fluids in the course of the measurements (Fig. 2.6(a)). This version of the liquid cell is ideal to measure tunneling currents through solvents or molecules which are chemically simple to handle. As a further development a bigger solvent reservoir was added to the liquid cell (Fig. 2.6(b)). This allows easy access for the addition of components in the solution and for the bubbling with argon. The bubbling will

be important to keep the solution free of oxygen, as it will be explained in Chapter 4. A tight contact of the cell to the sample surface is ensured via a spring for both versions of the cell.
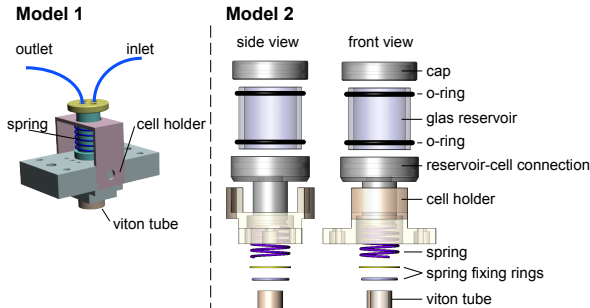

Figure 2.6: The two models of the liquid cell.

2.2.4 The autoranging low-noise I to V-converter

A 16-, and later 18-bit standard data acquisition board (National Instruments) is used both to apply a constant bias voltage and to record the current in the junction as measured by a custom-made auroranging low-noise current to voltage converter (AIVC, Fig. 2.7). This converter implements a fast automatic switching of the gain in between 10^5 and 10^8 V/A and enables measurements of conductance values ranging over many orders of magnitude, from the quantized conductance value of a single atom contact $G = G_0 = 2e^2/h$ [20; 32] down to $G \sim 10^{-7}G_0$ [77]. In other single molecule experiments [78] logarithmic I to V converters [79] are used, which also offer a dynamic range over several orders of magnitude. The disadvantage is that these logarithmic or quasi-logarithmic amplifiers have to be calibrated before starting the measurements and suffer from strong temperature sensitivity. In contrast, our amplifier does not need any calibration and is less sensitive to changes in temperature.

Prior to the input of the AIVC, a spike-killer (SK) is mounted. The SK is needed to reduce voltage spikes in the constriction, generated by the AIVC during range switching. The switching happens during the opening/closing of the junction, when the junctions are very sensitive and could be influenced by these spikes without the SK.
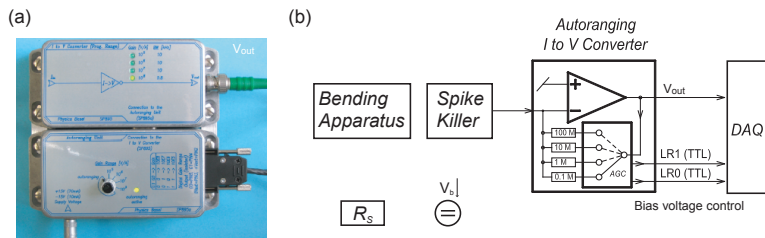
Figure 2.7: (a) Photo of the auto ranging I to V converter. (b) Schematics of the AIVC. The selected range is coded in a binary digital number (2 bit) and is sent to the DAQ. The spike-killer suppresses the unwanted spikes occurring during range switching at the input of the AIVC.

The input of the AIVC is virtually grounded. By using a good operational amplifier the input offset-voltage is typical below $\pm 100 \mu V$. The high DC voltage gain of the operational amplifier (around 10^6) leads to a very small DC input resistance of 0.1Ω for the 10^5 V/A range, respective 100Ω for the 10^8 V/A range. If AC measurements are performed around 400 Hz the input resistance is increased by a factor of ten due to the reduced AC voltage gain of the operational amplifier (constant gain-bandwidth product).

In addition to the analog output voltage from the AIVC of the junction the AIVC also generates two digital range lines. During an open/close-cycle the current flowing into the AIVC varies between the μA- and the pA-range. The AIVC selects automatically the optimal range between one of the four fixed linear gains of 10^5, 10^6, 10^7 and 10^8 V/A. For each of these gains one of four binary signal pairs is dedicated. These signals are recorded over the two digital range lines by the data acquisition system. By design the AIVC is inverting, which means the positive input currents result in negative output voltages.

The conductance of the junction (G_j) can be derived from the output voltage of the AIVC (V_{out}), the bias voltage (V_b), the series resistor (R_S), the voltage gain of the operational amplifier (A) and the selected linear range (LR) as following:

$$G_j = \frac{1}{\frac{V_b \cdot LR}{-V_{out}} - (R_S + \frac{LR}{A})} \tag{2.1}$$

The negative sign of the V_{out} in eq. 2.1 derives from the inverting character-

istics of the AIVC. For DC measurements, the term LR/A can be neglected since A is then around 10^6.

The achieved measurement resolution with the 18 bit data acquisition board, at a typical bias voltage V_b of 0.2V, yields $5 \cdot 10^{-5} G_0$ at a gain of 10^5 and $5 \cdot 10^{-8} G_0$ at a gain of 10^8. A more specified description of the AIVC can be found in Appendix A.

2.2.5 Grounding and shielding

The entire setup is isolated from the support (Fig. 2.8). To avoid ground loops, an isolation is inserted between the lateral shield of the setup and the grounded isolation of the BNC connectors. Furthermore the push-rod consists of an isolating material and the sample counter supports are isolated by a plastic foil. During the measurement the whole setup is shielded by an aluminum box. The typical current fluctuations are of $\pm 2.5 \cdot 10^{-12}$A in the lowest gain range.
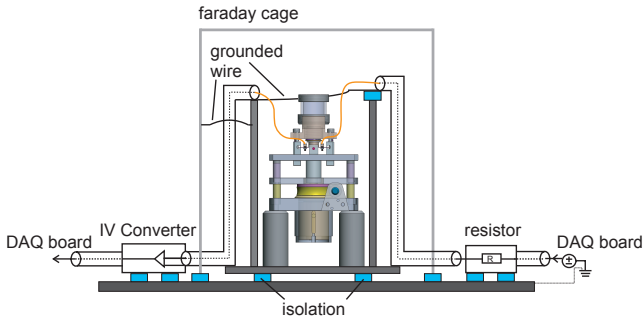
Figure 2.8: Grounding schematics of the break junction setup.

2.3 Sample fabrication on transparent substrates for optical purposes

As described in Section 1.7 one exhibits different alternatives to influence a molecule during a measurement. For light triggered experiments a UV lamp was used to illuminate the samples from the top. Another implementation of the light illumination is to reach a sample from the backside with a laser beam of a fluorescence microscope. With this goal, we explored the possibility of fabricating a break junction on a transparent substrate.

2.3.1 The choice of the substrate

The substrate for an optical break junction sample should have one major attribute: transparency. The second most important feature is its flexibility. Due to the common break junction fabrication process it needs to be resistant to certain chemicals (as acetone), high temperatures (175° C for lithography resist baking) and, for optical measurements, non fluorescent. Furthermore it should not be too expensive, because a given break junction sample survives only a reduced number of open-close cycles, before remaining permanently open. Considering all these parameters makes it difficult to find an adequate material. None of the materials we have found can fulfill all the desired characteristics. Nevertheless, relaxing our requirements we tested the two following substrates:

- Menzel Glass Covering Slips: The main problem of glass pieces is obviously its flexibility. Nevertheless, since it is possible to bend it for a small distance, we explored the feasibility of making the break junction gold bridge thin enough so that the bridge breaks before the glass substrate. These glasses are available in different thicknesses which are named with numbers: For our test samples we mainly used Nr. 1: (thickness 0,13-0,16 mm). We also did some tests with Nr. 0: (0,08 - 0,12 mm) and Nr. 2: (0,19 - 0,23 mm). Nr. 0 is too thin. It is very likely to break during sample preparation. Nr. 2 is to brittle. It breaks very fast when bending. Nr. 1 seemed to be the best in terms of preparation stability and bending curvature.

- Thermanox Coverslips: These coverslips are made of a polymer that is highly resistant to most chemicals. The polymer is flexible, transparent and has a temperature range of -70°C to +150°C. The main disadvantage is the autofluorescence in the range 380 to 545 nm and the great flexibility and softness which reduces the stability of a sample in the setup.

2.3.2 "Titanium" lithography

Optical lithography on glass or Thermanox substrates is approximately the same procedure as on spring steel substrates. The differences are as follows: 1. Instead of 90s, the resist is heated for 180 seconds at 90°C on the hotplate. The longer heating time, with respect to the metallic substrates, is needed due to the reduced heat transfer in the glass substrate. 2. During the exposure of only 20 seconds the substrate is mounted on a black base which protects the sample of excessive backscattered light.

E-beam lithography is more difficult. The electrons of the beam that exposes the sample need to flow out of the sample again. On conducting metal samples this can happen via the metallic sample holder. However, on insulating glass or plastic samples the electron beam produces charges, since electrons can not flow off the sample. This effect would make focusing and patterning by e-beam lithography impossible. To prevent the sample from charges, we found the solution of evaporating an additional layer of 30 nm titanium on the sample. Thanks to this layer, the rest of the e-beam lithography parameters vary very little with respect to the metallic substrates. In general a higher dose is needed. After exposure and development of the structure, the Ti/Au metal layer is deposited as usual directly on the undercoating Ti layer.

To finish the sample, the additional Ti layer that covers the whole substrate surface has to be removed by wet etching. After ~ 40 s in an etching solution (HF (10%), H_2SO_4 (30%), water, 1:1:40) the Ti layer is completely removed, leaving the break junction gold structure on the insulating substrate. At the same time the narrow part of the junction is under etched (note that working with HF is especially dangerous and needs adequate safety clothes). A SEM picture of break junction structure on glass is shown in Fig. 2.9.
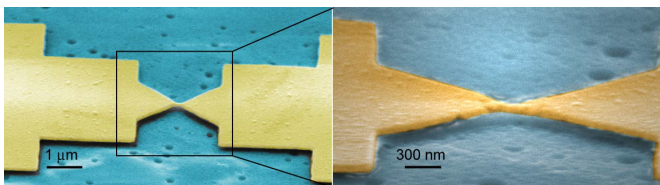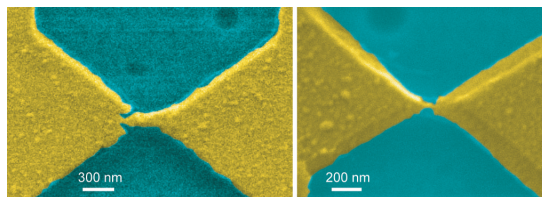

Figure 2.9: SEM image of a break junction structure on a glass substrate.

2.3.3 Electromigration

With the method of the "titanium" lithography we achieved gold bridges of ~ 50 nm. As mentioned before, the maximum stress before fracture of the glass is limited. Hence, in order to be able to operate the break junction we need a suspended bridge as narrow as possible, so it will break before the glass. To increase the chance of a working break junction sample we tried to decrease the width of the bridges by electromigration (EM). EM is the directed migration of atoms caused by a large electric current density. It proceeds by momentum transfer from electrons to atoms and requires sufficient atom mobility to occur. The effect of EM is used in Molecular Electronics to fabricate nanogaps between which molecules can be anchored and electrically measured [80; 81; 82]. Starting from a narrow metallic junction, EM narrows the junction down until a gap forms and the process self-terminates. With the proper control to stop EM before the gap opens we aim to use EM to narrow down the bridge of the break junction. The necessary current to start EM is achieved by applying a voltage U_0 over the break junction structure. As EM starts shrinking the junction, the resistance of the constriction R_J increases. To control the EM process properly it would be desirable to measure the resistance R_J. However, in lithographically-made break junctions the contact pads are far away from the constriction leading to long leads with resistances R_L, much larger than the resistance of the junction R_J. Due to the series resistance of R_L and R_J the change of R_J during the EM process is barely determinable.

For first tests we performed the EM process in an electron microscope (Philips SEM, XL-30) to monitor (by eye) the progress of the migration. The applied voltage U_0 was controlled manually. This slow control often lead to a "burn-through" of the junction. Nevertheless we were able to shrink down some of our break junction samples on glass (Fig. 2.10).

To better control the EM a process without the electron microscope would be desired. This would become possible with a proper measuring of the junction resistance R_J. To eliminate the problem of the lead resistances, we designed four terminals to each junction. In further work Wu *et al.* [83] developed a 4-terminal EM procedure in which an analog electronic feedback is controlling the junction voltage. Once EM has been initiated the junction gradually shrinks in size. It is demonstrated that narrow gaps can be obtained in a reliable and fast way under ambient conditions with yields approaching 100%. If the EM process is stopped just before the gap is opening one can expect a very narrow constriction.

Figure 2.10: SEM image of a break junction structure on a glass substrate after the electromigration process. The EM current is controlled by hand and the process monitored in the SEM.

2.3.4 Breaking glass Samples

As described above very nice-looking break junction structures were made on glass substrates, but unfortunately we were not successful in operating the glass break junction. The glass substrates were first cut with a diamond cutter to the appropriate size (1 cm x 2.4 cm), which might have damaged the glass on its borders leading to additional strains. The bending of the glass deteriorates these damages even more and leads to a fast breaking of the glass. Another impact are the contacts pressing on the glass samples. Note that we could reach the theoretical limit in "breaking" tests, though at a very low yield. The bending radius of the samples could be increased by using slender samples, e.g. 0.3 cm x 2.4 cm. Due to the incompatibility with our setup and liquid cell this test was not carried out.

Thermanox was rejected because of its oversized flexibility, the still inadequate chemical compatibility (e.g. tetrahydrofuran in molecule solvents), the lean heat resistivity, and the autofluorescence in the range 380 to 545 nm

2.4 Sample modification to reduce leakage currents

Measuring in a liquid environment always holds the problem of leakage currents through the liquid between the two contacts. The leakage current is proportional to the area of the contacts exposed to the liquid. To reduce the maximal area of the structure in liquid we produced a prototype sample which is for the most part covered with polyimide. This process is illustrated in Fig. 2.11(a).

1. It starts with a not under etched break junction sample.

2. Then a stripe of UV-resist is placed by UV lithography on the middle part of the structure. The UV-resist is needed because parts of the additional polyimide layer tends to stick on the gold even when etching a long time with the RIE machine (Appendix F). As a prototype mask for the UV lithography served a simple piece of aluminum foil with a slit inside, made with a diamond cutter. The mask was then aligned manually under the microscope. The width of the obtained UV-resist stripe is $\sim 50~\mu$m.

3. After development a layer of polyimide is spun on the sample. The large contact pads are covered with a piece of parafilm to keep them clean. In any case, this part of the gold will not be exposed to the solvent. The sample is then pre-baked at 200°C for 40 minutes and annealed at 390°C for 1 hour in a vacuum oven.

4. Finally, the polyimide on the sample is etched in the RIE machine. The parameters are the same as mentioned in Section 2.1.2. Though, the sample was covered with the aluminum foil mask again to only etch the middle part of the sample. Due to the "double layer" of polyimid, the etching time was increased to 10 minutes to get an under etched bridge. A SEM image of the resulting polyimide covered break junction sample is shown in Fig. 2.11(b).

In first tests the prototype junction showed a reduction of the leakage current by a factor of ~ 5 (from $1.1 \cdot 10^{-5} G_0$ to $2 \cdot 10^{-6} G_0$ in ethanol). However, the breaking point of the junction was achieved at low bending of the substrate and the lifetime was only short. To give clear values of the reduction of the leakage current more tests with such junctions have to be done. Furthermore, the fabrication procedure needs to be optimized.
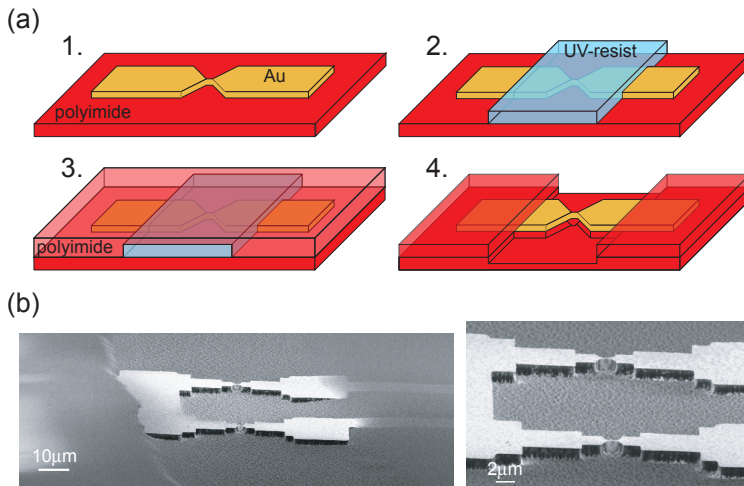
Figure 2.11: (a) How to fabricate a polyimide covered break junction sample to reduce the leakage current. (b) SEM image of the prototype sample.

Chapter 3

Investigation of "simple" molecules

To determine the feasibility of devices based on single molecules and to assess their properties, a single or a few molecules have to be wired in between two metal electrodes. This became possible only recently through different techniques such as scanning-probe microscopy, and mechanical and electromigration break junctions [20; 21; 23; 37; 84]. Using these techniques, the electrical conductances G of a broad range of molecular junctions have been determined [22; 39; 85; 86] and gating of single molecules has been demonstrated [63; 64; 81; 87].

Two different methods were first used to measure the electrical conductance through embedded single molecules, performing a statistical analysis. Either the contact to the molecule is fixed by STM on a self assembled mixed monolayer. The latter consists of an alkane layer fixed to the substrate by an anchoring group (eg. thiols) on one side of the molecule. The target molecule has two of those anchoring groups and sticks out of the alkane layer. The molecule is then contacted with the STM via a Au nano particle and the conductance is determined by measured I-V curves [21]. Or, the conductance can be measured by repeatedly opening and closing a junction and realizing many molecular junctions [23]. As shown in Section 1.4 a statistical analysis in the form of histogram is used to overcome junction-to-junction fluctuations. Peaks in the histogram point to preferred junction geometries. Evidence for the formation of few-molecules junctions is derived from the observation of a series of G values appearing at multiples of a fundamental single molecule value. Since in a break junction experiment the junction can be repeatedly opened and closed, we favor the second method.

In a previous work [38] we placed a C60 molecule with only one single

thiol anchoring group in our break junction setup and showed a resonant tunneling effect. However, to investigate the process illustrated above one needs a molecule with anchoring groups on both sides. An example experiment was performed by Xu *et al.* [23] on bipyridine molecules and thiolated alkane chains, both giving well defined peaks in the conductance histograms. Bipyridine (Fig. 3.1(a)) is a conjugated molecule and, in comparison to the alkane chains, a higher conductance is expected. Therefore the bipyridine molecule seems more interesting. Xu *et al.* show very clear and well defined bipyridine conductance peaks at $1 \cdot 10^{-3} G_0$ and on multiples of this value (Fig. 3.1(b)). Motivated by these results we carried out a test measurements with bipyridine molecules.

## 3.1 Electrical conductance of bipyridine

The bipyridine has two nitrogen atoms on both ends that can bind to gold electrodes (Fig. 3.1). The coordination of the pyridine nitrogen to the surface should depend on the surface potential of both electrodes with respect to a reference electrode. This potential dependent coordination has been observed in electrochemical STM investigations [88; 89]. With a positive surface potential, we establish an attraction between the electrode and the nitrogen lone pair. Thus, the pyridine nitrogen coordinates to the surface. Upon coordination, the π system of the heterocycle is expected to couple strongly with the electrodes fermi level. This coupling of the pyridine nitrogens to the electrodes is expected to provide an efficient electron transport between the two electrodes.

Our measurement was performed by repeatedly opening and closing the break junction immersed in a bipyridine solution while recording the conductance. The push-rod was moved at different velocities between $v_z = 10\,\mu\mathrm{m/s}$ and $v_z = 30\,\mu\mathrm{m/s}$, so that the two Au leads separate at $0.2 - 1.2\,\mathrm{nm/s}$. The concentration of the bipyridine in the solution was typically 1 mM (but also 0.5 mM and 5 mM was measured). As a solvent for the bipyridine we used DMSO and (following [23]) 0.1 M NaClO$_4$ and 0.1 M LiClO$_4$ aqueous solution [1]. To influence the surface potential, a silver wire, dipped into the molecular solution, served as gate electrode. We measured at bias voltages V_{bias} between +0.8 V and -0.8 V. Further the applied gate voltage U_{Ref} was changed between +0.6 V and -0.6 V. To analyze the data we built histograms of 100 consecutive conductance curves. Fig. 3.1(c) shows a representative histogram of our bipyridine experiments. We did *not* find any peaks in our examined conductance region. No matter what solvent we used, what sample bias or gate voltage we applied, no matter the concentration of the

---

[1]dissolving only possible with the help of a ultrasonic bath

bipyridine or the added salt, the expected feature of the bipyridine did not show up clearly in our histograms. The question to be asked upon this:
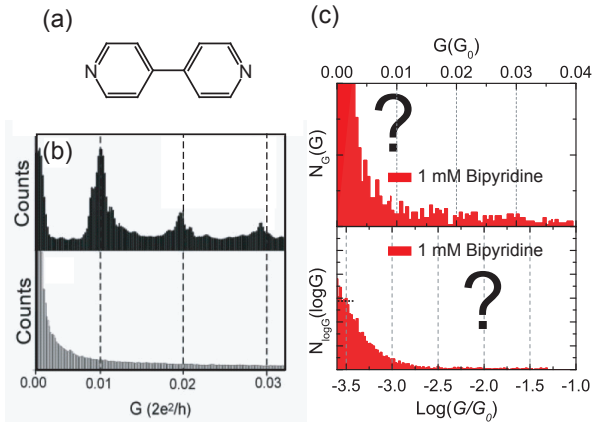

Figure 3.1: (a) structure of the investigated bipyridine molecule. (b) Xu *et al.* (Science, **301**, 1221) show a clear peak at 0.01 G_0 for bipyridine in a solvent (top) while no peak appears in a solvent only (bottom). (c) Our measurement of bipyridine shows no peak in the examined region. The histograms are constructed of 100 consecutive conductance curves. The upper histogram illustrated in linear scale, the lower histogram in log scale. Both histograms are built using the same data.

why? Several factors may play a role. In this preliminary measurements, we did not implement a reference electrode. In absence of latter, we do not control the potential properly. Although we can change it by the potential on the silver wire, we do not control it. The wrong surface potential will inhibit the coordination of the pyridine nitrogen to the surface. Further, for these measurements we used an I to V converter with a fixed gain. This allows only a distinct window of conductance and further averts the control on how much the break junction is closed after each cycle. Further, due to the fast retraction of the gold leads when opening a fully closed break junction, it could be possible to miss the conductance feature.

The investigation of the conductance of bipyridine also led to an extensive discussion about the data analysis of the conductance measurements. Different groups [90; 91; 92] have applied different data selection schemes to resolve the peaks in the G-histograms. When trying to understand the

difficulties to reproduce results from different laboratories, it became an issue to establish which should be the standard data processing. The variety of methods and the convenience of performing any pre-selection of the measurements will be discussed in Section 3.2.

Here we analyze a group of 60 G vs. z curves obtained for a solution of 1 mM bipyridine in DMSO. Using the data analysis as suggested in [91], we did a pre selection of curves with plateaus. Fig. 3.2 (a) illustrates the selected single conductance curves. The plateaus are highlighted in black. In (b) we built a histogram with the mean values of the selected plateaus weighted by their lengths. The histogram shows a peak at 0.01 G_0 which is similar to Xu *et al.* [23]. This peak is absent for the measurement without the bipyridine (c). Note that we found plateaus in both measurements, with and without the bipyridine. These results were not reproducible, and only one out of 20 measurements showed clear plateaus.
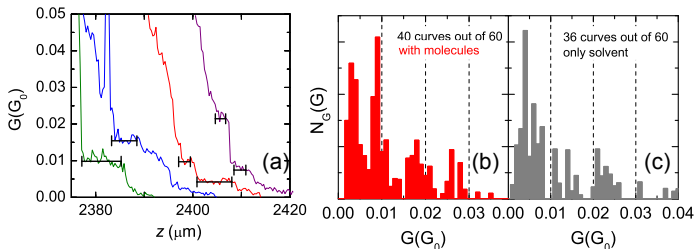
Figure 3.2: (a) Example of selected conductance curves. The plateaus are highlighted in black. (b) Histogram of the mean plateau value weighted by its length. (c) Histogram of a measurement in solvent only.

In conclusion we were not able to successfully determine the conductance of the bipyridine molecule in our break junction setup. The chain of reasoning is to test an even simpler molecule and led to the decision to measure the octanedithiol. The thiol anchoring groups are expected to bind strongly to gold, without any potential dependencies.

Further, the situation with various analysis methods applying different selection criteria to construct the conductance histograms is unsatisfactory. A method without any selection would be preferential. Thus, we will address this important question in the next Section and introduce a new robust statistical analysis method on the basis of octanedithiol measurements.

3.2 Electrical conductance of octanedithiols

As a second test case, we have chosen octanedithiol junctions [21; 23; 69; 91; 92; 93; 94]. We compared conductance histograms, which were generated with and without data selection. We show that the conductance value assigned to a single molecule is *robust* and that data selections do not help to improve the results. The most convincing representation is found in a histogram of $\log G$ rather than G.

The measurements were performed at room temperature, in a liquid environment. The push-rod was moved at a velocity $v_z = 30\,\mu\text{m/s}$, so that the two Au leads separate at $0.5 - 1.2\,\text{nm/s}$. We apply a constant bias voltage of $0.2\,\text{V}$, and record the variation of the current I through the junction during repeated open-close cycles. The current was measured with the autoranging low-noise I to V-converter described in Section 2.2.4. This allows us to register the conductance variation during the whole process, starting from the fused Au junction with $G > G_0 := 2e^2/h$, until the formation of single molecule junctions, with conductance values orders of magnitude lower.
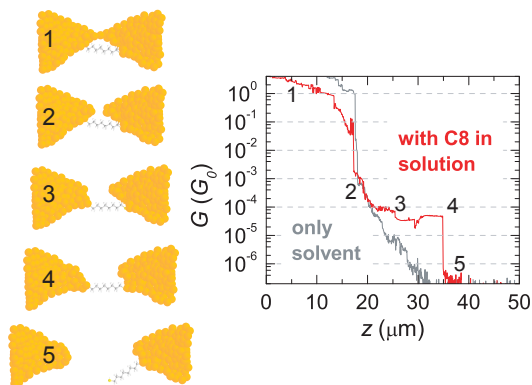
Figure 3.3: Breaking process of a break junction in liquid environment with C8 molecules present.

In Section 1.3 we described the breaking process in a solvent where no other molecules are present. Here we show how we figure the breaking process and what we expect from a measurement when molecules link the gap. The red curve in Fig. 3.3 shows the variation of the break junction conductance during a typical breaking process immersed in a solution of

thiolated C8 molecules. It evolves in several steps. In the high conductance regime above 1 G_0 it behaves similar to the breaking process in a solvent alone. Although molecules might be present, the conductance is dominated by the gold contact (1). After the Au bridge breaks, the gold contacts retract, leading to a fast drop in conductance. Even though a molecule may link in between, the conductance is dominated by the tunneling current due to the short distance between the Au-Au contacts (2). At some point after increasing the gap between the contacts the tunnelling current along the molecule gets perceptible (3). If molecules are anchored in between the gap, we call it molecular junction. In that case another plateau in the $G(z)$ curve is anticipated [23; 40]. Similar to atomic junctions, this metal-molecule-metal bridge holds via its chemical bonds the two sides together and postpones the breaking open of the Au electrodes (3 to 4). Finally, the molecule loses contact and the conductance decreases (5).
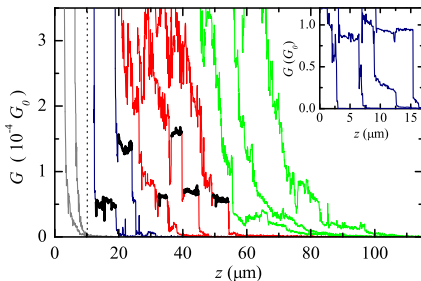
Figure 3.4: Variation of conductance during the breaking process of a junction in pure mesitylene (left of the vertical pointed line), and in a solution of octanedithiol in mesitylene (right). The curves are shifted in z for clarity. In the presence of octanedithiol, 50 % of the curves present plateaus. From these, some are very clean (the two first ones from left - blue), and others are noisier (the following three ones - red). The remaining 50 % (the last three ones - green) show an irregular decay without plateaus. The plateaus have been highlighted in black. Inset: Examples of plateaus close to 1 G_0, corresponding to one-atom gold contacts.

In order to explore process explained above, we have performed groups of 100 consecutive open-close cycles for 5 different samples, both in pure mesitylene and in a 1 mM solution of octanedithiol in mesitylene. In Fig. 3.4, we show a group of representative $G(z)$ curves during opening of the bridge. Whereas the curves in the main panel focus on values in the low conductance regime, i.e. at $G \approx 10^{-4} G_0$, the inset shows data around $G \approx G_0$,

corresponding to the single-gold-atom contact. Whereas $G(z)$ decays in an exponential fashion in the pure solvent (curves to the left of the dotted line), distinct plateau features may appear in octanedithiol containing solution, as explained previously in Fig. 3.3. In some curves, jumps between plateaus at different G can be seen. In those cases, the molecular junction reorganizes, and the number of bridging molecules may change. In Fig. 3.4, the first two curves (blue) to the right of the vertical dotted line, are rather 'clean'. In contrast, the three next curves (red) are quite noisy just before plateau formation. This suggests that there is a large degree of molecular movement in the junction, until the octanedithiol molecules eventually lock in between the leads. Finally, some $G(z)$ curves measured in the presence of molecules do not display plateaus (last three curves in green). In this case, no stable single-molecule bridge has been formed. Such traces correspond to approximately 50% of the curves.

Now, we focus on the statistics of our measured data. For each sample, we take all 100 conductance traces $G(z)$ and determine the probability with which a particular G-value is measured, $p_G(G)$. This is depicted in the conductance histograms of Fig. 3.5(a) (bin size: $\Delta G = 4 \cdot 10^{-6}\,G_0$). Whereas $p_G(G)$ decays smoothly in the pure solvent, there are distinct peaks appearing in the octanedithiol case (indicated by arrows). This suggests that particular molecular configurations form with a high probability. However, the peaks in Fig. 3.5(a) are masked by a strong background. One may therefore wonder, whether a particular data processing method could improve the sharpness of the peaks. In the literature, different procedures have already been used, but they have not been compared carefully yet. In forming histograms, the proposed procedures consist of: a) disregarding $G(z)$-curves that do not present clear plateaus [67; 90]; b) only using data points that belong to plateaus, instead of taking the whole $G(z)$ data [69]; c) only using average values derived from the data points belonging to conductance plateaus and weighing these by the plateau length [91]; and d) using conductance jumps [92]. In focusing on the plateau values, these methods do effectively eliminate a background. However, they can be objective, as they involve decisions as how constant the signal has to be to define a plateau, or where the plateau starts and ends exactly.

3.2.1 The alternative analysis method

We propose an alternative method, which does not make use of any data selection. We take all data, and only subtract a background that is adapted to the physics of the problem. This method is as powerful as all of the previous ones and, most importantly, it is fully objective. In proceeding, we note that the conductance must contain a tunneling contribution [10]. The

tunneling conductance G is exponentially dependent on the gap distance d, i.e., $G \propto \exp(-2\kappa d)$. Here, $\kappa = \sqrt{2m\phi}/\hbar$ is the decay constant, ϕ the apparent barrier height, and m the electron mass. Furthermore, $d = a(z - z_0)$, where a is the attenuation factor of the MCBJ [8; 10], and z_0 is defined as $z(d = 0)$. Rewriting this, we find $\ln G = -2\kappa a z + const$. It seems therefore much more appropriate to plot histograms of $\ln G$ rather than of G.

Making use of this expression, we can now calculate which is the expected tunneling contribution in the conductance histograms. If we denote with p_G, $p_{\ln G}$, and p_z the respective probabilities of measuring a certain value of G, $\ln G$ and z, we may write

$$p_G(G)\, dG = p_{\ln G}(\ln G)\, d\ln G = -p_z(z)\, dz. \qquad (3.1)$$

Here, $p_z(z) = R/v_z$, where R is the data acquisition rate, and v_z is the velocity of the vertical push-rod. In our case, both these quantities are constant: $R = 500$ points/s, $v_z = 30$ μm/s. Solving eq 3.1 for $p_{\ln G}$ yields

$$p_{\ln G}(\ln G) = \frac{R}{2\, v_z \kappa\, a}. \qquad (3.2)$$

Consequently, $p_{\ln G}$ is constant, whenever ϕ and a are constants. Hence, in a $\ln(G)$- or $\log G$-histogram, tunneling shows up as a constant background which is easily subtracted. For a detailed analysis of the transformation between log- and linear histograms see Appendix C. In Fig. 3.5(b), we show a $\log G$-histogram built from the data in Fig. 3.5(a) (bin size: $\Delta \log(G/G_0) = 5 \cdot 10^{-3}$). A constant background is indeed present for $G \lesssim 2 \cdot 10^{-4}\, G_0$ for the pure solvent (blue line), for which tunneling is the only expected contribution. In contrast, clear peaks appear in the presence of octanedithiol. The $\log G$-histogram representation is very powerful for another reason: it presents a full overview of the data. At a glance, both the single-atom Au contact peaks ($G \approx G_0$) and the molecules signal ($G < 10^{-3}\, G_0$) are seen. Between 10^{-2}–$10^{-3}\, G_0$ (depending on the sample) and G_0, there is almost no weight in the histograms. This indicates that the Au atoms retract quickly immediately after breaking the gold atom bridge, as was already shown in Fig. 3.3 (position from 1 to 2). The tunneling background, which is constant in a $\log(G)$-histogram, is inversely proportional to G in a G-histogram, the latter being the representation the literature focused on so far. Solving eq. 3.1 for p_G yields

$$p_G(G) = \frac{R}{2\, v_z \kappa a} \frac{1}{G}. \qquad (3.3)$$

As can be seen in Fig. 3.5a, this expression perfectly matches the G-histogram
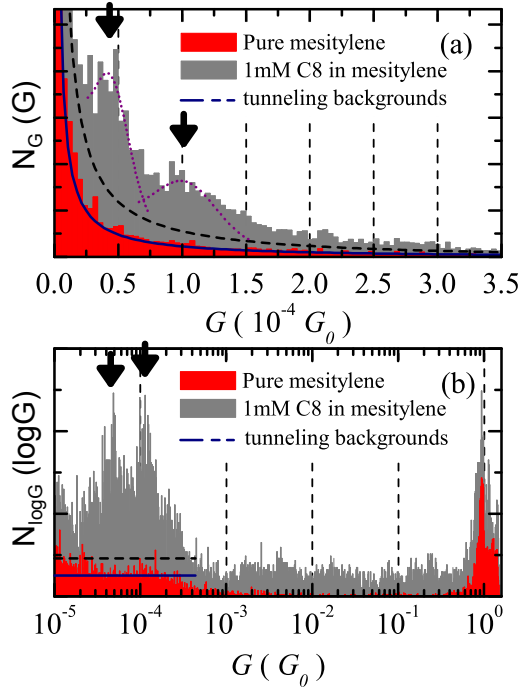
Figure 3.5: (a) Conductance histograms built from approximately 100 $G(z)$ curves (Fig. 3.4) in pure mesitylene (red), and in a solution 1mM of octanedithiol (grey). The arrows indicate the conductance peaks that appear when octanedithiol is added in solution. The blue and black-dashed lines show the best fit from below using a expression $\propto 1/G$ to both histograms.(b) Histograms of $\log G$ built from the same data as in (a). The blue and black-dashed lines correspond to the same $R/(2\,v_z\kappa a)$ values as in (a). Note that in the latter representation both atomic gold peaks and molecule peaks are observed.

of the pure solvent. The blue-line backgrounds of Fig. 3.5a and b correspond to the same $R/(2\,v_z \kappa a)$.

We can use this property to subtract the tunneling background for the histograms on dithiol molecules. To this end, we fit eq 3.3 to our data from below. This background is shown in Fig. 3.5(a) (black-dashed line). The same $R/(2\,v_z \kappa a)$ gives the black-dashed constant background in Fig. 3.5(b). Subtracting it from the data yields a corrected histogram which is guided by the physics of tunneling. The result of this subtraction is shown in grey in Fig. 3.6 (main panel and insets), for two different samples. Fig. 3.6(a) corresponds to the data of Fig. 3.5. From this analysis we conclude that junctions with conductance values at multiples of $4.5 \cdot 10^{-5}\,G_0$ are more favorably formed. This number is then assigned to the conductance of a single Au-octanedithiol-Au bridge, G_1.

We will next compare our background subtraction method with other approaches based on curve selection. This comparison is shown in Fig. 3.6. The blue-line histogram has been obtained by taking only curves in which plateaus are apparent (i.e. the blue and red curves in Fig. 3.4). In the red dashed histogram only the points within a plateau have been used. The latter data selection scheme is highlighted in black in Fig. 3.4. The selection was done manually and no other treatment was applied. Comparing these three histograms, it is quite striking that all exhibit the same key features. There are two, sometimes even three conductance peaks at multiples of the same G-value (i.e., $G_1 \approx 4.5 \cdot 10^{-5}\,G_0$). Of special interest is the similarity of the grey and blue-line histograms in Fig. 3.6. We conclude from this that the $G(z)$ curves without apparent plateaus can, on average, be described by a tunneling dependence. The effective barrier height in this case is somewhat smaller than in the pure solvent. The third, red dashed histogram, in which only plateau values were considered, also yields similar peak positions but appears to have an even stronger background subtracted. This is expected as in this histogram the noisy signals away from the plateaus (as shown in the red curves of Fig. 3.4) have been removed.

From the histograms, we find a single molecule conductance $G_1 \approx 4.5 \cdot 10^{-5}\,G_0$. In literature, values ranging from 1 to $25 \cdot 10^{-5}\,G_0$ have been reported [21; 23; 69; 91; 92; 93; 94]. Our value lies very close to the one found by Wandlowski *et al.* [69]. It is also close to that of Steigerwald *et al.* [95] for octanediamine in trichlorobenzene ($2 - 6 \cdot 10^{-5}\,G_0$), which was obtained without the need for data selection. This similarity is particularly remarkable considering the different bounding group of the molecules. Tao *et al.* [91] reported two groups of peaks at multiples of $G_L = 5.2 \cdot 10^{-5}\,G_0$ and multiples of $G_H = 2.5 \cdot 10^{-4}\,G_0$. They attributed these to two distinct microscopic arrangements of the molecule-S-Au bonds. Whereas the first value agrees well with our findings, we do not observe any other peak at
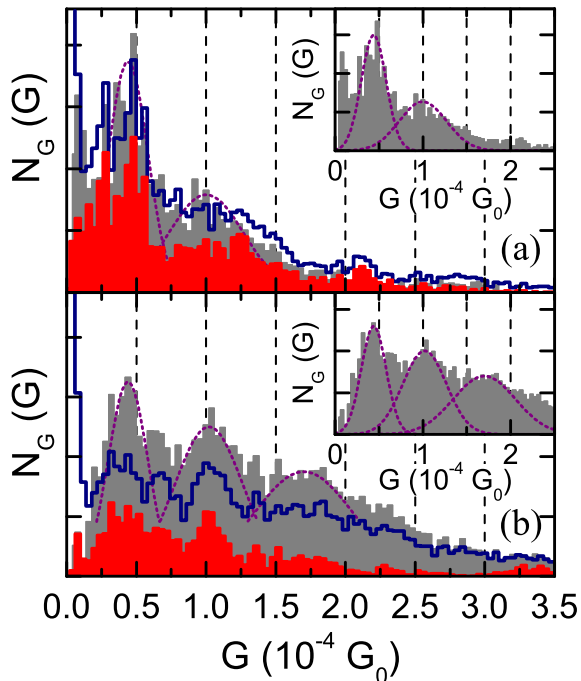
Figure 3.6: Histograms built from a given group of $G(z)$ curves. (a) and (b) show results for two different samples. The grey histograms were obtained considering all the measured conductance traces, and subtracting later the tunneling background (also shown in the insets). The blue-line histograms were made with the curves that display clear plateaus (blue and red curves in Fig. 3.4). Finally, the red histograms were built only with the G values which belong to plateaus (marked in thick black in Fig. 3.4). The Gaussian curves highlight the position of the peaks.

higher conductance values. This is especially made clear by the $\log(G)$-histogram of Fig. 3.5b. The different solvent used in their work could be a possible cause for the formation of the second group of peaks. However, Tao *et al.* [91] observed peaks at the same conductance values in different solvents. Another notable difference between the two experiments is the speed at which the junctions are opened: $40\,\mathrm{nm/s}$ in the work of Tao *et al.* [91], and $1\,\mathrm{nm/s}$ in our case. We speculate that the change in speed

could lead to the detection of different microscopic conformations. Finally, a given microscopic arrangement could also be favored in our symmetric MCBJ, in comparison with the more asymmetric junctions formed in a STM configuration.

3.2.2 Conclusion

From the above discussion, it is clear that a detailed analysis of conductance histograms is required to gain insight into the microscopic formation of single molecule junctions. In the analysis methods employed so far, a data selection process has been used. In contrast, we demonstrate that a simple background subtraction scheme suffices. It is as powerful as any data selection schemes and, in contrast to the latter, it is objective. We emphasize that the statistical analysis is most conveniently performed in a histogram in which $\log G$ is represented. The $\log G$ representation allows a simple background subtraction and provides an overview from the single atom contact to tunneling. Moreover, the single (few) molecule conductance values show up in a much more striking manner. In addition, we conclude that the features appearing in the conductance histograms obtained with break junctions (in MCBJ or STM configuration) are robust and can be realistically attributed to the molecular signature in these junctions.

Chapter 4

Investigation of conjugated oligomers

4.1 Introduction

In the previous chapter we successfully stablish the conductance value for a molecular bridge based on octanedithiol molecules and introduced a robust statistical analysis method. Using these tools, we feel confident to study other more complex molecules. Doing small steps, we moved on to conjugated molecular wires.

In particular, we will study molecular rods consisting of a conjugated backbone between terminal anchor groups allowing for immobilization in a junction. Prototype conjugated molecules of this kind are oligo(phenylene vinylene) and oligo(phenylene ethynylene) with sulfur anchoring groups for which we will be using the shorthand OPV and OPE in the following. There have been studies on self-assembled monolayers using scanning tunneling and atomic-force microscopy [96; 97; 98], but most of the work on such kind of molecules has been done for relatively large-area junctions, realized for example by crossed-wires [99; 100], electrochemically-grown nanowires [101; 102], nanopores [103], or Au colloid arrays [104]. In those cases, one has to estimate the number of molecules in the junctions, which is prone to errors. Only three studies of OPE compounds could address single-molecule transport properties directly [39; 67; 105].

As a result, the absolute conductance values obtained for OPE and OPV compounds still span about two orders of magnitude. Previous work point to a higher conductance of OPV as compared to OPE [97; 99; 101], but there also exists a large variation in the ratio, ranging from a factor of two to as much as ten.

In the following Section, we present quantitative measurements of the electrical conductance G of both OPE and OPV molecules using mechanically controllable break junctions (MCBJ) in a controlled liquid environment [10]. These measurements directly provide an assessment and a comparison of the single-molecule conductance values of OPE and OPV under identical conditions. We compare OPV with OPE and two modified OPE's on which solubilizing side groups were added [106]. We find that OPV conducts better than OPE, but the difference is modest with typical conductance values of 2.0 and $1.2 \cdot 10^{-4} G_0$ for OPV and OPE, respectively.

4.2 Experimental part

To determine the electrical conductance of the molecular junctions, a voltage bias of $0.2\,\text{V}$ [1] is applied between the left and right contact and the resulting current is measured with the custom-made AIVC. To assess the conduc-
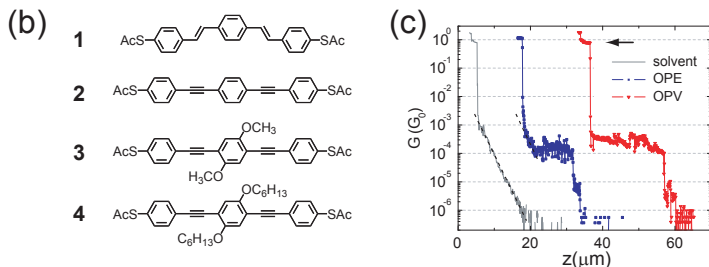
Figure 4.1: (a) Structures of the molecules examined in this study. **1**: oligo(phenylene vinylene) (OPV) and **2-4**: oligo(phenylene ethynylene)'s (OPEs). (b) Typical measurements of the electrical conductance $G(z)$ as a function of push-rod movement z during an opening cycle in the pure solvent (grey), and in the same solvent to which conjugated molecules were added (blue and red).

tance G of the conjugated molecules, the junction is periodically opened and closed, as explained in Section 3.2, in the presence of a $0.25\,\text{mM}$ solution of molecules **1-4** (Fig. 4.1(a)) in a mixture of THF/Mesitylene (1:4 v/v-ratio) (henceforth the solvent). $100\,\mu\text{M}$ tetrabutylammonium hydroxide (TBAH) was added to the solution to remove the acetyl protection groups *in-situ* in the liquid cell. The TBAH concentration ensuring a proper deprotection was established via thin layer chromatography (TLC). Upon deprotection

---

[1] Note that the current-voltage characteristic is linear in this low-voltage regime.

the molecular solution changes color from bluish transparent to a bright yellow. During the measurements the solution was kept under Ar atmosphere to prevent the deprotected bifunctional molecules from polymerization via disulfide bond formation. Following the procedure described in Chapter 3, 100 open-close cycles define one set of measurement. For all molecules, at least three sets of measurements using different samples have been acquired.

Fig. 4.1(b) presents three $\log G(z)$ curves, representative for the solvent alone (grey curve) and conjugated OPE/OPV molecules (blue and red curves). With respect to the single conductance curves of octanedithiol, they hold longer plateaus, with larger fluctuations.

We find it more appropriate to discuss the measured $G(z)$ values in a $\log G$ representation, because only this representation is able to provide an overview of the junction conductance during the whole breaking process. As we showed in Chapter 3, it is straightforward in the $\log G$ representation to determine a pure tunneling background that can be subtracted without affecting the conclusion. This is because a tunneling dependence in $G(z)$ results in a constant contribution to the $\log G$-histogram, whereas a (noisy) plateau, as the ones shown in Fig. 4.1(b), produces a (broad) peak (see e.g. Fig. 4.2(b)), which we identify as the signature of the anchored conjugated molecules. The width of this peak reflects the fluctuations in the molecular junctions, caused for example by the switching of the molecules between different binding sites (hollow, on-top, or bridge site) [91; 93]. As we will show below, the peaks in the $\log G$-histogram appear to be surprisingly symmetric, suggesting that the fluctuations are approximately Gaussian around a central value in the log-representation.

4.3 Results

Fig. 4.2 shows a set of representative conductance histograms measured for molecules **1-4**. These are compared with histograms obtained for two references, which are octanedithiol molecules (C_8) in mesitylene (Chapter 3) and the solvent alone. Fig. 4.2(a) emphasizes on the comparison using a $\log G$ representation. In contrast to the solvent, there appear pronounced, nearly symmetric peaks on a relatively flat background in a conductance window around 10^{-4} to $10^{-3}\,G_0$ for C_8 and **1-4**. As mentioned above, these peaks are the signature of molecules that are trapped in atomic-sized junctions. Focusing on the central weight of each peak, we see that molecule **1** (OPV) conducts best, followed by molecules **2-4** (OPEs). In contrast, the reference compound C_8 has clearly a lower conductance value. Taking different measurement sets into account, we can hardly resolve a difference between the three kinds of OPE molecules. We therefore conclude that the
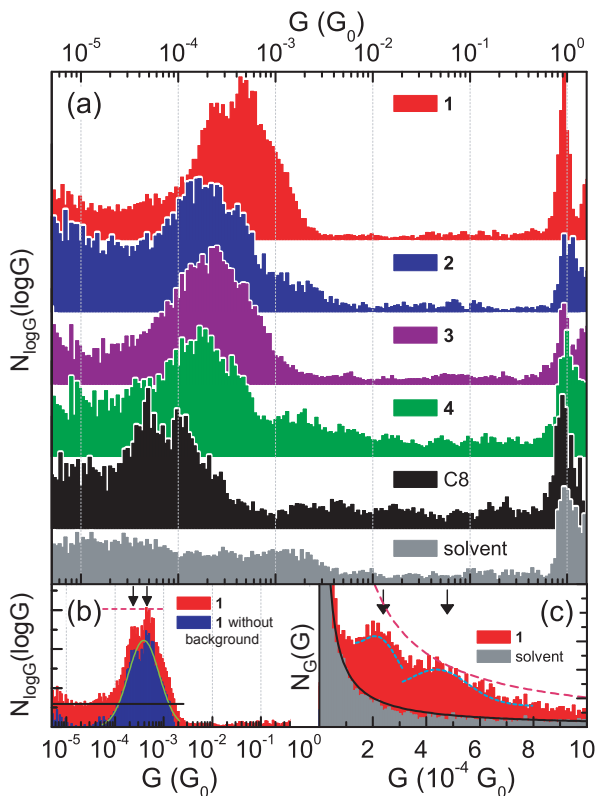
Figure 4.2: (a) Log-histograms of measured conductance values $log(G(z))$ obtained during one hundred successive open cycles similar to those three examples shown in Fig. 4.1(b). From top to bottom, the histograms show data for OPV **1** (red), OPE compounds **2-4**, and the two references, octanedithiols in mesitylene (black) and the solvent alone (grey). (b) A $log\,G$-histogram of an OPV measurement that shows a fine structure (arrows) in addition to the gross Gaussian-like peak (green curve) that spans about one order of magnitude. In the linear G-histogram representation (c), the fine structure appears as a pair of peaks spaced by a factor of two. (c) also shows that the solvent alone yields a background that follows a $1/G$ dependence (grey). For the measurement with OPE/OPV molecules, the background is deduced as a constant value at the low G side of the $log\,G$-histogram (black horizontal line in (b)) which transforms into the $1/G$ dependence in the G-histogram shown as a solid curve in (c).

side groups at the central phenyl ring, added to increase solubility, have no measurable effect on the electron transfer. We emphasize here that the side groups in compounds **3** and **4** do apparently not prevent the molecules from anchoring within the junction. It is also interesting to note that the width of the molecular signature in the $\log G$-histograms are similar for all anchored molecules. Because of the strong difference between OPE/OPV and C_8 molecules, we suggest that the width is to a great extent caused by fluctuations in the particular anchoring comprising S-Au bonds [107]. In addition to 'bare' fluctuations leading to a wide conductance peak, a fine structure, consisting of a set of multiple peaks, can be superimposed. An example of an OPV measurement is shown in Fig. 4.2(b), where the two arrows point to the fine structure with two peaks. We also emphasize that the visibility of this fine structure varies from sample to sample displaying no fine structure, one, two and sometimes even three peaks (Fig. 4.5). As explained in Section 3.1, these 'satellite' peaks are attributed to the formation of multiple molecular bridges [21; 23]. Because the conductance value for a molecular junction consisting of n-molecules bridging the gap in parallel is expected to be n-times the single-molecule G-value, the fine structure is better analyzed in a linear representation, where multiples of a fundamental value can more easily be determined. This is illustrated in Fig. 4.2(c), where the same OPV data set as in Fig. 4.2(b) is plotted. The fine structure consists in this case of two peaks, which indeed appear approximately at conductance values that agree with a single molecule junction for the lower conductance peak and a double-molecule junction for the higher one. In the same graph we also plot the tunneling background on the low G side (black curve), which follows a $1/G$ dependence as stated in Chapter 3. It can best be determined from the $\log G$-histogram at the low-G side as a constant value (shown as a black horizontal line in Fig. 4.2(b)).

More explicitly, the conversion from the $\log G$-histogram, $N_{logG}(logG)$, to the linear one, $N_G(G)$, is given by

$$N_G(G) = N_g(g)\frac{log(e)}{G}\frac{\Delta G}{\Delta g} \qquad (4.1)$$

where ΔG and Δg denote the (constant) bin-size in the G- and $\log G$-histogram, respectively. This relation (explained in detail in Appendix C) transforms the shape of the molecular features in a distinct manner. The gross molecular signal, which appears as a relatively wide Gaussian-like peak in the $\log G$-histogram is converted into a highly asymmetric peak in the linear histogram. Because of the large width of the molecular signal in the $\log G$-histogram, which spans an order of magnitude in G values, the major contribution in the linear histogram comes from the central part where

N_{logG} is approximately constant, leading to a tail that follows approximately an $1/G$ dependence (see dashed curve in Fig. 4.2(c) and the corresponding dashed line in Fig. 4.2(b)).

4.4 Discussion

To quantitatively analyze our data, we proceed along two alternative methods.

4.4.1 Method (a)

In method (a), we base our analysis on the gross molecular signature seen in the $\log G$-histogram. We first subtract the low-G background to the left of the peak and then fit a Gauss function to the remaining peak (this procedure is highlighted with the curve in Fig. 4.2(b)). To determine the center value, we first transform this Gauss function from the logarithmic to the linear representation. The molecular signal in the $\log G$-histogram can
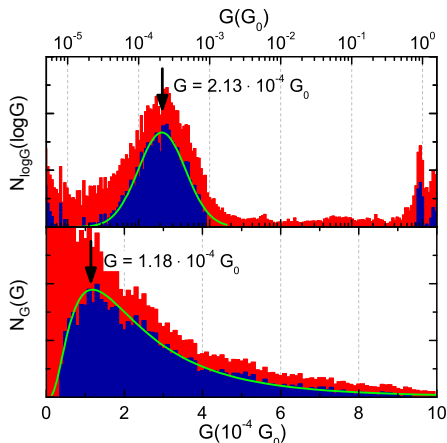
Figure 4.3: (a) Log plot of a measurement of **2** including the fitted Gauss curve having the width $w_g = 0.33$, and a peak maximum appearing at $2.13 \cdot 10^{-4} G_0$. The horizontal line shows the subtracted background. (b) linear plot of the same data, including the transformed Gauss function as described in the text. The maximum is shifted to the left, located at $1.18 \cdot 10^{-4} G_0$.

be approximated by a Gauss function, i.e. we fit $N_g(g)$ according to:

$$N_g(g) = C \exp\left(-(g - g_c)^2/2w_g^2\right) \ , \tag{4.2}$$

where w_g denotes the width, g_c the center value, and C a constant. This Gauss function is transformed into the linear G-histogram, using eq 4.1, i.e.:

$$N_G(G) \propto \frac{exp\left(-(logG - g_c)^2/2w_g^2\right)}{G} \ . \tag{4.3}$$

This transformation is explicitly illustrated in Fig. 4.3. The position of the maximum in the $\log G$-histogram is by definition g_c. After the transformation to the linear histogram, the peak position is however not found at the value $G_C = 10^{g_c}$, but it is shifted to a lower value, given by:

$$log(G_c) = g_c - ln(10)w_g^2 \ . \tag{4.4}$$

This can be derived by setting the derivative of eq 4.3 to zero and solving for $logG$. The symmetric peak in the $\log G$-histogram gets thereby strongly skewed. The low conductance side of the peak is compressed to values close to zero, leading to a sharp increase on the left, whereas the high conductance side is stretched into a long tail with approximate $1/G$ dependence.

Fig. 4.4 shows the data of molecules **1-4** in the most interesting region in the form of a linear G-histogram for G-values in the range from $3 \cdot 10^{-5}G_0$ to $10^{-3} G_0$. The tunneling background, appearing at low G values (the $1/G$ dependence shown as a solid curve in Fig. 4.2(c)), has been subtracted for all set of measurements. The dashed curve represents the transformed Gaussian fits. It is quite remarkable how good this function describes the overall distribution visible in the linear G-histogram. Because of this very good agreement, we use the value G^a of the peak position of the transformed curve as a measure of the single-molecule value determined by method (a). We note that this is one particular choice.

4.4.2 Method (b)

Whereas method (a) emphasizes the overall molecular signal visible in the $\log G$-histogram, method (b) now focusses on the fine structure, which is better visible in the linear G-histograms. This second analysis assumes that the histogram is made up of contributions from junctions with one, two or a multiple of molecules bridging the gap in parallel. We then assume that the peak positions of the fine structure occur at multiples of a fundamental value, which we term G^b. We use a multi-Gaussian fit (dotted curves in Fig. 4.4) with up to four Gauss peaks centered at multiples of G^b. The first peak has the width w^b at half maximum. In order to reduce the number of
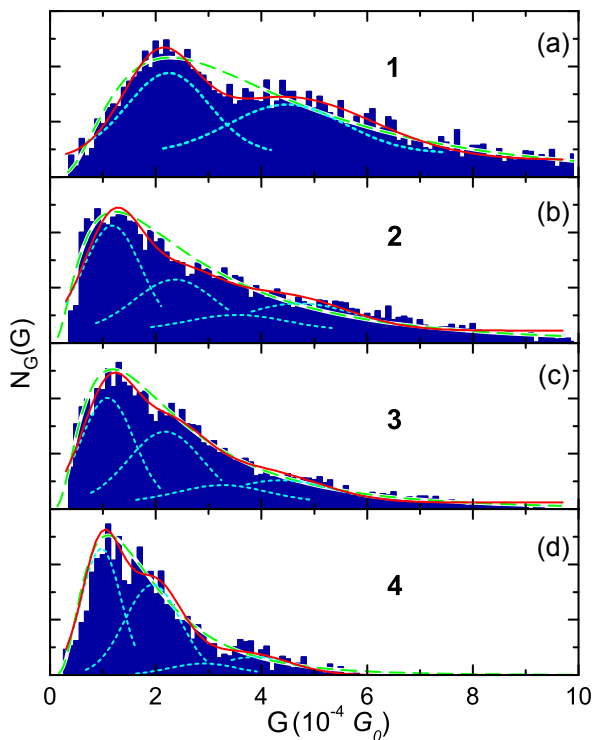
Figure 4.4: Four representative measurements of molecules **1-4** in linear-scale G-histograms with subtracted background. The dotted curves (blue) correspond to the components of the multiple Gaussian-peak fits, resulting in the solid curves (red). The dashed curves (green) have been obtained from a Gauss function fitted to the overall peak visible in the log G-histogram (see for example the green curve in Fig. 4.2(b)) which are then transformed onto the linear-scale G-histogram.

fitting parameters, we assume in addition that the width of successive peaks grows with the square-root of the number of molecules in the junction. The red solid curves in Fig. 4.4 correspond to the result of this procedure. Due to the large number of parameters, it is not too surprising that a good agreement results. We stress however, that independent of this procedure, major peaks are visible without applying a fitting procedure. The fitting procedure only serves to assess numbers in an objective manner.

4.4.3 Sample-to-sample variation

After describing the fitting and analysis procedure, we can discuss the sample dependent variances of measurements in the $\log G$-histogram.

Fig. 4.5 shows three histograms for OPV built each from 100 conductance traces from three distinct samples. All three histograms present a first maximum around $2 \cdot 10^{-4} G_0$ whereas a second maximum only develops clearly for the first two sam, with even a third maximum appearing for sample 1 (sample 2 corresponds to the data shown in Fig. 4.2). This shows that multiple bridges can appear with different probabilities, which we attribute to different local geometries of the metal electrodes.
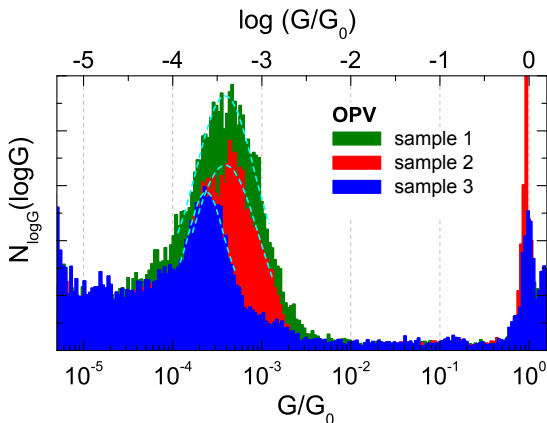
Figure 4.5: Possible conductance peak dispersion in the $\log G$ histograms for example measurements of OPV.

Following method (a) we fit Gaussian curves (blue dashed lines) in the $\log G$ histograms of Fig. 4.5, thus obtaining the peak value g_c and the width w. Now we can use the transformation between the log- and linear scale

histograms as explained eq. 4.4. Hence, we obtain the conductance values G_c in the linear scale. The values for g_c, w and G_c are given in Table 4.1. The

Samples	g_c $log(G_0)$	w_g $log(G_0)$	G_c $10^{-4}G_0$
Sample 1	-3.42	0.34	2.2
Sample 2	-3.41	0.33	2.1
Sample 3	-3.62	0.18	2.0

Table 4.1: Values for g_c, w and G_c obtained from the gauss fits in Fig. 4.5. A dispersion in the $\log G$-histogram g_c values is found. After the transformation to the linear G-histogram, the G_c values are approximately the same.
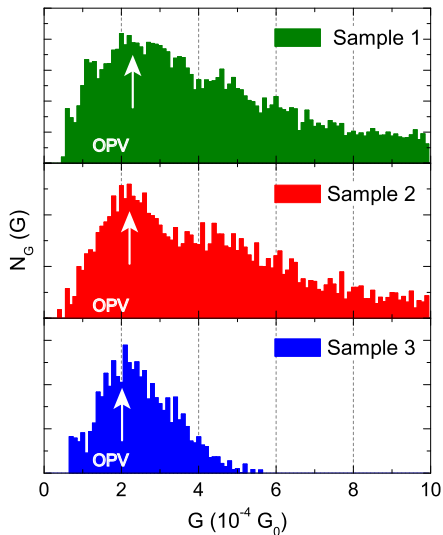
Figure 4.6: Linear histograms of the same three samples shown in Fig. 4.5. The white arrows highlight the value of the transformed peak from the log histogram gauss fits.

molecular signatures of samples 1 and 2 in Fig. 4.5 look pretty much the same and it is therefore not surprising that the transformation gives similar values. Nevertheless, also the transformation of the sample 3 data corresponds to the first two. The smaller shift is due to the sharper peak width w. To

support the calculations from above, the same data of the $\log G$-histogram in Fig. 4.5 is illustrated in $linG$ in Fig. 4.6. The white arrows highlight the values calculated above. Additional data for OPE measurements can be found in Appendix E.

4.4.4 Conductance values comparison

We can now plot the main results in Table 1, which are average single-molecule conductance values G^a and G^b, obtained by method (a) and (b) for molecules **1-4**, as well as the width at half maximum w^b. First, it is clear that w^b is of the same size as the mean conductance value itself. Second, there is a remarkable agreement between G^a and G^b values. This coincidence is surprising and was not anticipated.

molecule	# of samples	G^a $(10^{-4}G_0)$	G^b $(10^{-4}G_0)$	w^b $(10^{-4}G_0)$
1	5	2.0 ± 0.2	2.1 ± 0.2	1.7
2	5	1.2 ± 0.1	1.2 ± 0.2	1.1
3	4	1.2 ± 0.1	1.2 ± 0.1	1.1
4	3	1.2 ± 0.2	1.1 ± 0.1	1.0

Table 4.2: Average single-molecule conductance values $G^{a,b}$ for molecules **1-4**, obtained with method (a) and (b), respectively. Whereas G^a is deduced from fits to the overall peak in the $\log G$-histograms, G^b focusses on the fine structure which is better visible in the linear G-histograms. In addition, the full-width at half maximum w^b of the single-molecule peak obtained from the linear histograms is given as well. All numbers show a higher G-value for OPV than OPE.

The OPE molecules (**2-4**) all yield identical single-molecule conductance values of $G_{OPE} = 1.2 \cdot 10^{-4}G_0$, in good agreement with the single molecule measurements of Xiao *et al.* [67]. Calculations predict however substantially larger absolute values (more than an order of magnitude) for OPE of $2.4 \cdot 10^{-3}G_0$ [108] and $2.1 \cdot 10^{-2}G_0$ [109]. Our comparison on the single-molecule level of OPE with OPV shows that OPV conducts slightly better. We obtain $G_{OPV} = 2 \cdot 10^{-4}G_0$, or expressed in terms of a ratio, $G_{OPV}/G_{OPE} \simeq 1.7$. Whereas the absolute values in first principle calculations deviate substantially, one can obtain agreement in the relative numbers. Paulsson *et al.* have calculated the conductance values for both OPV (**1**) and OPE (**2**) and find a ratio of 1.7 between OPV and OPE, in excellent agreement with our result [109]. On the experimental side, our OPV value agrees with a recent AFM study on OPV molecules inserted into an alkanethiol self-assembled monolayer by Seferos *et al.* who reports 15.8 ± 6.9 nS, which converts to $G_{OPV} \approx 2 \cdot 10^{-4} G_0$ [98].

We can try to explain the conductance ratio between OPV and OPEs, assuming the simplest possible model (Section 1.6.4) for the electron transfer, which is single-step through-molecule tunneling with a square potential-barrier determined by the HOMO-LUMO gap E_g. Then, G is given by $G = A exp(-2\sqrt{2\phi m}d/\hbar)$, where m is the electron mass, d the length of the molecule measured between the sulfur atoms, ϕ the barrier height, assumed to be half of E_g, and A a constant determined by the Au-S bond, which should therefore be equal for all molecules.

We determine an average HOMO-LUMO gap $\overline{E_g}$ for each molecule from the optical UV-vis adsorption spectra. Fig. 4.7 shows the UV-vis adsorption spectra of compounds **1-4** measured in dichlormethane. It is seen that the spectrum of OPV looks remarkably similar to the one of OPE, except that the former is red-shifted by $\sim 30\,\text{nm}$, due to the higher conjugation of the pi-electron system in OPV.
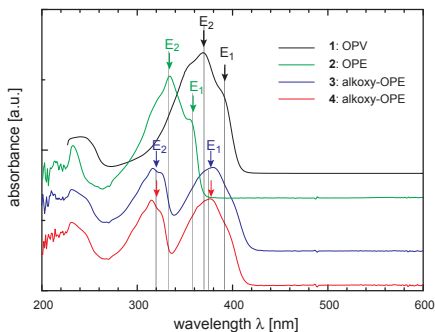
Figure 4.7: UV-vis adsorption spectra of compounds **1-4** measured in dichlormethane.

The OPE molecules with alkoxy substitutions in the 2,5 position of the central phenyl ring display a different adsorption spectrum. Whereas for OPV and OPE two peaks overlap, which are visible as a dominant peak and a weaker shoulder at longer wavelength, the two peaks markedly split apart for the modified OPEs. This has been described in the work of James *et al.* [110] who assigned the peaks to two close-lying HOMO orbitals. To deduce an effective HOMO-LUMO gap E_g for the electron transfer, we determine the energies $E_{1,2}$ of both transitions (arrows) from the wavelengths $\lambda_{1,2}$ at the center of the peaks. We assume that the electron transfer probability is given by $T(E_g) = Ae^{(-2\sqrt{mE_g}d/\hbar)}$ with a constant A, meaning that both orbitals

couple equally to the electrodes. The average gap $\overline{E_g}$ is then obtained from the following equation: $T(\overline{E_g}) = \frac{1}{2}(T(E_{g1}) + T(E_{g2}))$. We obtain $\overline{E_g} = 3.2$ for OPV **1**, 3.5 for OPE **2**, 3.44 eV for the two OPEs **3, 4** with side groups (sg-OPEs).

Taking OPE as our reference conductance value, this simple approach then predicts that OPV should conduct 3.6 times better, while the sg-OPEs should only conduct 1.5 times better. Here we have used a fixed distance $d = 2.0$ nm for all molecules. The predicted sequence, that the OPEs have similar conductance values and the OPV is conducting better, is well reproduced in the experiment. We note, however, that the relaxed sulfur-sulfur distance of OPV should be slightly shorter than that of OPE. This would increase the ratio G_{OPV}/G_{OPE} to values > 4. This discrepancy may be resolved if we take the force into account which is constantly pulling on the partially flexible molecule and thereby increasing the actual distance between the terminal anchor groups, possibly in a different manner for OPE and OPV. It may also be possible that the different rigidity of the two molecules in the axial direction yields different thermal fluctuation amplitudes, affecting the average conductance values.

Finally, one cannot stress enough the uncomfortable situation that there is considerable disagreement in the conductance value of such a simple molecule as the OPE. Whereas early experiments by Reichert *et al.* and Mayor *et al.* yielded a very large conductance value of $G_{OPE} \simeq 2.5 \cdot 10^{-3} G_0$ [39; 105], a recent single-molecule STM study reports a value of only $2.6 \cdot 10^{-5} G_0$ [106], with our value $G_{OPE} \simeq 1.2 \cdot 10^{-4} G_0$ lying somewhere in between. Even larger values of $G_{OPE} \simeq 10^{-2}$ and $G_{OPV} \simeq 4 \cdot 10^{-2} G_0$ were reported by Kushmerick *et al.* [99] using crossed-wire junctions. In this latter case it is however likely, that many molecules were measured in parallel.

4.5 Conclusion

In conclusion, we have compared the molecular signature of four different conjugated molecules in break junctions at the single molecule level and under identical environmental conditions. We find a larger conductance value of $2 \cdot 10^{-4} G_0$ for OPV as compared to three OPE compounds, which all show a conductance of $1.2 \cdot 10^{-4} G_0$. Our data suggest that the three phenyl rings are close to planar, even in the presence of the solubilizing side groups, maximizing the conjugation. We have also put forward a new method to analyze conductance values G based on a histogram of the logarithm of G. In such a histogram, all the weight that can be assigned to the presence of molecules anchoring in the gap yields a symmetric peak, whereas the data

in a linear G representation is a strongly asymmetric peak that assumes a power-law dependence over almost the whole range of G-values, closely following $1/G$.

Chapter 5

Engineered molecules

As mentioned in the introduction, molecules may become an alternative for silicon based integrated circuits. As described in the last two chapters, there is a great activity in comprising "simple" molecules in nano contacts. Though, to become suitable for an application, it is essential to synthesize and investigate molecules with a distinct implemented electronic function. Recently, molecular rectifiers [42; 111; 112] or hysteretic switching [43; 113] deriving from embedded molecules have been reported. Further light triggered photoreactions [48; 73; 74; 75] or electrochemically active chromophores [68; 114; 115; 116] have been used or proposed. Also, integrated molecules reacting with an analyte have been reported [76; 117] as switches or potential sensing devices. Furthermore there is a good amount of review papers on functional molecules [72; 118; 119; 120] showing the fascinating activity in the field.

5.1 Cruciform molecules

Grunder *et al.* [121] proposed and synthesized a new form of molecules having the potential of a molecular switch. This molecule consists of two rod like π systems crossing each other (see Fig. 5.1) and both rods are able to bridge the gap between the contacts. The difference is that the two rods exhibit a different surface dependent behavior. While one of the rods (an OPV) contains thiol end groups, the second one (an OPE) is functionalized terminally with pyridine subunits. The OPV rod with the thiol anchoring groups is mainly there to hold the molecule inside the gap. In contrast the

OPE rod with the pyridine anchor group is the active part of the switch. As explained in Section 3.1, in an electrochemically controlled junction, the coordination of the pyridine nitrogen should depend on the surface potential of both electrodes with respect to a reference electrode (see Fig. 5.1(b)). Upon coordination, the π system of the heterocycle is expected to couple strongly with the electrodes fermi level. In contrast to that, the sulfur bonds provide a considerable tunnel barrier for electronic transport [122; 123]. With a negative surface potential respect to the reference electrode, both pyridine groups are not coordinated to the surface. This is due to the repulsion between the electrode and the nitrogen lone pair. Therefore only the OPV rod binds to the electrodes. When moving U_{Ref} towards a positive potential the repulsion changes to an attraction and the pyridine nitrogen starts to coordinate to the surface. Thus the electron transport between the two states should alter considerably. Even more, this switching process is expected to be reversible, since the surface dependent coordination is reversible.
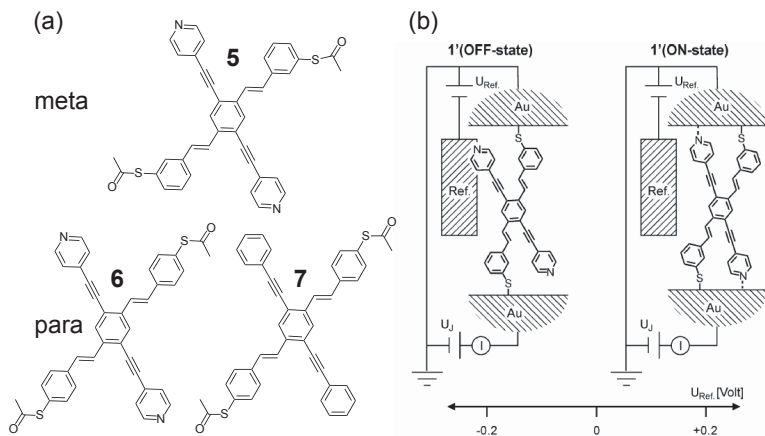
Figure 5.1: (a) Three different cruciform molecules. **5** contains the thiol anchoring group at meta position, **6** and **7** at para position. Further cruciform **7** is lacking the pyridine nitrogen. (b) Switching mechanism in an electrochemical setup. Depending on the surface potential the pyridine nitrogen coordinates or does not coordinate to the electrode surface.

5.2 Measurement of cruciform molecules

Before attempting any switching, we have to show the immobilization on single molecule level between the contact electrodes. Due to the structural complexity and spatial extensions of the cruciform structures **5 - 7**, it can be first of all unclear whether they can be contacted for transport characterization. However, note that we immobilized an OPE molecule with long side groups (**4**) in the previous chapter, which is a good starting point to try molecules **5 - 7**.

For these measurement of the cruciform molecules, no significant changes respect to the technique used in Chapter 4 were introduced. Hence, the cruciform molecules were dissolved in a mixture of THF/Mesitylene (1:4 v/v-ratio) at a concentration of 0.25 mM and incorporated to the liquid cell. The acetyl protection groups of the thiophenol anchor groups were removed in situ by adding 50 μl of a 10 mM solution of tetrabutylammonium hydroxide (TBAOH) in THF. The molecular solution is kept under argon atmosphere by constantly bubbling with argon to suppress any oxygen-promoted oxidation process like disulfide formation.

For this measurements, about 200 consecutive open-close cycles for each solution were recorded. The corresponding histograms are shown in Fig. 5.2(a) following the procedure introduced in Chapter 3. No molecular signature could be detected for cruciform **5**. Although OPE rod-type structures with sulfur anchor groups in the meta position have been investigated in a MCBJ setup in vacuum [105], similar characteristics of the OPV backbone with sulfur anchor groups in the meta position were not observed in the liquid environment. We expect that the OPV subunit exhibits a conductance below our detection threshold ($\sim 10^{-6} G_0$). This is reasonable, since Mayor *et al.* [105] show a decrease of conductance of two orders of magnitude by changing the anchoring group of an OPE molecule from para to meta position.

However, the two molecules comprising the para-thiolated OPV backbone have been integrated successfully and their conductance histograms, as well as the one of the solvent, are displayed in Fig. 5.2(a). The measurement of the solvent only shows a peak at 1 G_0 which belongs to the mono atomic gold contacts. In contrast, both cruciform molecules **6** (red) and **7** (dark gray) display a clear molecular signature in the tunnel region of the conductance histogram. We relate this signature to the OPV substructure of these cruciform molecules which links to the Au leads by forming covalent S-Au bonds. Comparing to the OPV (**1**) measurement of Chapter 4 (also shown in Fig. 5.2(b)) the similarity between the histograms for **1** and **6** is quite striking. Both show two marked peaks at $2.2 \cdot 10^{-4} G_0$ and $4.4 \cdot 10^{-4} G_0$ which are attributed to one and two molecules in parallel immobilized in the junction. The histogram recorded with cruciform **7** shows also a clear peak in
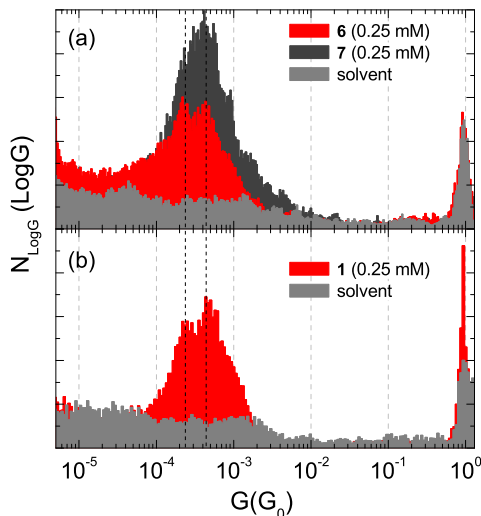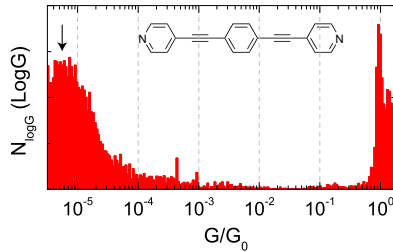
Figure 5.2: (a) Conductance histogram for the pure solvent (gray), **6** (red) and **7** (dark gray). The histograms are made out of 200 consecutive conductance curves. (b) Characterization of OPV (**1**) as a reference compound. The same data is shown in Chapter 4. The solvent was a 0.17 MM TBAOH solution in THF/mesitylene (1/4).

the same conductance regime, with the first two peaks being more blurred. We have also seen in Section 4.4 that the visibility of the fine structure on the molecular signature of OPV can vary in the same degree from sample to sample (Fig. 4.5). Anyhow, the first peak is still observable by a shoulder at $2.2 \cdot 10^{-4} G_0$.

As a second control experiment an OPE rod comprising terminal pyridine groups, as the second rod-like subunit of cruciforms **5** and **6**, has been investigated under the same conditions. As shown in Fig. 5.3(a) molecular signature appears below $10^{-5} G_0$ while no molecular signature can be observed in the conductance regime of the cruciform molecules. This further corroborates that the OPV substructure is the trapped structure. The measured molecular signature in Fig. 5.3 is surprising, since we were not able to immobilize the bipyridine molecule in Chapter 3.

If we assume a conductance of $10^{-5} G_0$ for the OPE like rod and estimate the conductance for an OPV and OPE molecules in parallel, the change

Figure 5.3: (a) Conductance histogram for the OPE rod comprising terminal pyridine groups. While a peak appears below $10^{-5}G_0$ there is no signature around $2 \cdot 10^{-4}G_0$

in conductance will not be larger than $\sim 10\%$. This small difference in conductance between the open and closed position of the molecular switch, will be very hard to distinguish. Taking this into account Grunder *et al.* will synthesize a next generation of cruciforms, whereas a considerably increased difference between both states is hypothesized.

5.3 Conclusion

These measurements demonstrate that designed molecular structures with significant complexity can be immobilized in a MCBJ setup in liquid environment. The latter offers further the possibility to implement the required reference electrode to control the surface potentials of both electrodes to be able to investigate the switching potential of these molecular junctions.

Chapter 6

Conclusion and Outlook

In this thesis we successfully investigated the electrical conductance of different single molecules. As an experimental setup, we used a mechanically controllable break junction technique with an implemented liquid cell, allowing measurements in a liquid environment.

We started with "simple" molecules to achieve a good understanding of the electrical conductance of molecular junctions. With the investigation of the conductance of octanedithiol molecules, we were able to contribute to the discussion concerning the conductance value of a single octanedithiol measured in different laboratories. We further proposed a new statistical analysis method. While different groups have applied data selection schemes to resolve peaks in G-histograms, our method does not need any selection.

After this introductive investigation of a simple molecule, we continued with more complex molecules. Thus, we measured and compared the conductance of different conjugated oligomers. We find that oligo(phenylene vinylene) (OPV) conducts slightly better than oligo(phenylene ethynylene)'s (OPEs), expressed in terms of ratio, $G_{OPV}/G_{OPE} \simeq 1.7$. Our data suggest that the three phenyl rings are close to planar, maximizing the conjugation.

Finally, we prove that a newly designed molecular structure, having the potential of a molecular switch, with significant complexity, can be immobilized in our MCBJ setup. This measurement further shows that, from the two arms of this molecule, the arm ended by thiols (and not the one ended by nitrogen) is the one anchoring. The expected switching could not be shown yet, due to experimental limitations.

Regarding our break junction samples and setup, we were able to considerably decrease our samples fabrication time, while increasing the yield of

working samples. By implementing a new autoranging I to V converter, we can continuous measure the conductance of a break junction from several G_0 down to $\sim 10^{-6}G_0$. This was important to get a good control over the breaking process of a break junction. Further we developed a liquid cell, allowing an easy access to the molecular solution during a measurement.

The focus for future work will be preferential on molecules with a distinct implemented electronic function. Therefore the new task will be to implement the proper potential control to the existing setup. Further different solvents (eg. different electrolytes) for these measurements have to be tested. Also the break junction sample itself needs an improvement: to reduce the possible undesirable leakage currents in solvents, the gold area exposed to the solvent needs to be covered as good as possible with an insulating layer.

It could be very interesting to have a deeper look into different anchoring groups of molecules, e.g. the molecules measured in Chapter. 4. Further, it would be interesting to investigate how the electrical conductance of OPE or OPV will vary when removing one or even two phenyl units from the molecular structure. Although experiments on comparable molecules have been done [37; 107], a comparison of OPE or OPV with different lengths at a single-molecular level is still missing.

In our measurements in liquid many molecules are around the junction. These molecules may have an influence on each other, eg. by Van der Waals interaction or $\pi - \pi$ stacking. We could therefore study intermolecular interactions.

In my early diploma work [124] I fabricated palladium break junction and investigated the conductance of atomic Pd contacts in different solvents. It could now be interesting, to use these palladium break junction for molecular measurements.

List of Figures

List of Tables

Bibliography

[1] G. E. Moore, Electronics **38**, 8 (1965).

[2] H. Kuhn and D. Möbius, Angew. Chem. Int. Ed. **10, no. 9**, 620 (1971).

[3] A. Aviram and M. A. Ratner, Chem. Phys. Lett. **29**, 277 (1974).

[4] J. Moreland and J. W. Ekin, J. Appl. Phys. **58**, 3888 (1985).

[5] C. Zhou, C. J. Muller, M. R. Deshpande, J. W. Sleight, and M. A. Reed, Appl. Phys. Lett. **67**, 1160 (1995).

[6] J. M. van Ruitenbeek et al., Rev. Sci. Instrum. **67**, 108 (1996).

[7] L. Grüter, *Mechanically controllable break junction in liquid environment: a tool to measure electronic transport through single molecules*, PhD thesis, University Basel, 2005.

[8] S. A. G. Vrouwe et al., Phys. Rev. B **71**, 035313 (2005).

[9] C. Untiedt et al., Phys. Rev. B **66**, 085418 (2002).

[10] L. Grüter, M. González, R. Huber, M. Calame, and C. Schönenberger, Small **1**, 1067 (2005).

[11] J. K. Gimzewski and R. Möller, Phys. Rev. B **36**, 1284 (1987).

[12] J. C. Maxwell, *A Treatise on Electricity and Magnetism, Vol. 1*, Dover Publications, 1954.

[13] Y. V. Sharvin, Sov. Phys.-JETP **21**, 655 (1965).

[14] S. Datta, *Electronic Transport in Mesoscopic Systems*, Cambridge University Press, Cambridge UK, first edidtion edition, 1995.

[15] R. Landauer, Phil. Mag. **21**, 863 (1970).

[16] R. Landauer, Phys. Scr. **T42**, 110 (1992).

[17] E. Scheer, P. Joyez, D. Esteve, C. Urbina, and M. H. Devoret, Phys. Rev. Lett. **78**, 3535 (1997).

[18] J. M. Krans et al., Phys. Rev. B **48**, 14721 (1993).

[19] J. M. Krans, J. M. van Ruitenbeek, V. V. Fisun, I. K. Yanson, and L. J. de Jongh, Nature **375**, 767 (1995).

[20] N. Agraït, A. Levy-Yeyati, and J. M. van Ruitenbeek, Phys. Rep. **377**, 81 (2003).

[21] X. D. Cui et al., Science **294**, 571 (2001).

[22] R. H. M. Smit et al., Nature **419**, 906 (2002).

[23] B. Xu and N. J. Tao, Science **301**, 1221 (2003).

[24] G. Binnig and H. Rohrer, Helv. Phys. Acta. **55**, 726 (1982).

[25] C. J. Muller, J. M. van Ruitenbeek, and L. J. de Jongh, Phys. Rev. Lett. **140**, 1992 (69).

[26] C. J. Muller, J. M. van Ruitenbeek, C. W. J. Beenakker, and R. de Bruyn Oubote, Physica B **189**, 225 (1993).

[27] N. Agraït, J. G. Rodrigo, and S. Vieira, Phys. Rev. B **47**, 12345 (1993).

[28] J. I. Pascual et al., Phys. Rev. Lett. **71**, 1852 (1993).

[29] L. Olesen et al., Phys. Rev. Lett. **72**, 2251 (1994).

[30] G. Rubio, N. Agraït, and S. Vieira, Phys. Rev. Lett. **76**, 2302 (1996).

[31] J. C. Cuevas, A. L. Yeyati, and A. Martín-Rodero, Phys. Rev. Lett. **80**, 1066 (1998).

[32] E. Scheer et al., Nature **394**, 154 (1998).

[33] C. Joachim, J. K. Gimzewski, R. R. Schlittler, and C. Chavy, Phys. Rev. Lett. **74**, 2102 (1995).

[34] M. Dorogi, J. Gomez, R. Osifchin, R. P. Andres, and R. Reifenberger, Phys. Rev. B **52**, 9071 (1995).

[35] L. A. Bumm et al., Science **271**, 1705 (1996).

[36] R. P. Andres et al., Science **272**, 1323 (1996).

[37] M. A. Reed, C. Zhou, C. J. Muller, T. P. Burgin, and J. M. Tour, Science **278**, 252 (1997).

[38] L. Grüter et al., Nanotechnology **16**, 2143 (2005).

[39] J. Reichert et al., Phys. Rev. Lett. **88**, 176804 (2002).

[40] H. B. Weber et al., Chem. Phys. **281**, 113 (2002).

[41] J. Reichert, H. B. Weber, M. Mayor, and H. v. Löhneysen, Appl. Phys. Lett. **82**, 4137 (2003).

[42] M. Elbing et al., PNAS **102**, 8815 (2005).

[43] E. Lörtscher, J. W. Ciszek, J. Tour, and H. Riel, Small **2**, 973 (2006).

[44] R. Ochs, D. Secker, M. Elbing, M. Mayor, and H. B. Weber, Faraday Discuss. **131**, 281 (2006).

[45] J. J. Park et al., Phys. Rev. Lett. **99**, 026601 (2007).

[46] E. Lörtscher, H. B. Weber, and H. Riel, Phys. Rev. Lett. 98, 176807 (2007) **98**, 176807 (2007).

[47] C. Kergueris et al., Phys. Rev. B **59**, 12505 (1999).

[48] D. Dulić et al., Phys. Rev. Lett. **91**, 207402 (2003).

[49] J.-H. Tian et al., JACS **128**, 14748 (2006).

[50] http://www.monos.leidenuniv.nl/smo/index.html?basics/photophysics.htm.

[51] A. Nitzan, Annu. Rev. Phys. Chem. **52**, 681 (2001).

[52] F. Zahid, M. Paulsson, and S. Datta, *Electrical Conduction in Molecules*, Academic Press, 2003, Chapter published in "Advanced Semiconductors and Organic Nano-Techniques".

[53] J. M. Tour, Chem. Rev. **96**, 537 (1996).

[54] M. Magoga and C. Joachim, Phys. Rev. B **56**, 4722 (1997).

[55] S. B. Sachs et al., J. Am. Chem. Soc. **119**, 10563 (1997).

[56] K. Pettersson et al., J. Phys. Chem. A **110**, 310 (2006).

[57] C. Atienza et al., Chem. Comm. , 3202 (2006).

[58] M. D. Newton, Chem. Rev. **91**, 767 (1991).

[59] H. M. McConnell, J. Chem. Phys. **35**, 508 (1961).

[60] M. A. Ratner, J. Phys. Chem. **94**, 4877 (1990).

[61] C. Goldman, Phys. Rev. A **43**, 4500 (1991).

[62] C.-P. Hsu and R. A. Marcus, J. Chem. Phys. **106**, 584 (1997).

[63] A. R. Champagne, A. N. Pasupathy, and D. C. Ralph, Nano Letters **5**, 305 (2005).

[64] S. Kubatkin et al., Nature **425**, 698 (2003).

[65] M.-H. Jo et al., Nano Letters **6**, 2014 (2006).

[66] F. Chen et al., Nano Letters **5**, 503 (2005).

[67] X. Xiao, L. A. N. amd A. M. Rawlett, and N. J. Tao, J. Am. Chem. Soc. **127**, 9235 (2005).

[68] Z. Li et al., Faraday Discuss. **131**, 121 (2006).

[69] Z. Li et al., Nanotechnology **18**, 044018 (2007).

[70] M. Irie and M. Mohri, J. Org. Chem. **53**, 803 (1988).

[71] M. Irie, T. Fukaminato, T. Sasaki, N. Tamai, and T. Kawai, Nature **420**, 759 (2002).

[72] B. L. Feringa, *Molecular Switches*, Wiley-VCH Verlag GmbH, Weinheim, Germany, 2001.

[73] J. He et al., Nanotechnology **16**, 695 (2005).

[74] S. J. van der Molen et al., Nanotechnology **17**, 310 (2006).

[75] T. Kudernac, S. J. van der Molen, B. J. van Wees, and B. L. Feringa, Chem. Comm. , 3597 (2006).

[76] X. Guo et al., Nano Letters **7**, 1119 (2007).

[77] M. Steinacher et al., The autoranging i to v converter, to be published.

[78] J. He et al., Faraday Discuss. **131**, 145 (2006).

[79] U. Dürig, L. Novotny, and B. Michel, Rev. Sci. Instrum. **68**, 3814 (1997).

[80] H. Park et al., Nature **407**, 57 (2000).

[81] J. Park et al., Nature **417**, 722 (2002).

[82] W. Liang, M. P. Shores, M. Bockrath, J. R. Long, and H. Park, Nature **417**, 725 (2002).

[83] Z. M. Wu et al., Appl. Phys. Lett. **91**, 053118 (2007).

[84] Z. J. Donhauser et al., Science **292**, 2303 (2001).

[85] A. Salomon et al., Adv. Mater **15**, 1881 (2003).

[86] R. L. McCreery, Chem. Mater. **16**, 4477 (2004).

[87] B. Xu, X. Xiao, X. Yang, L. Zang, and N. Tao, J. Am. Chem. Soc. **127**, 2386 (2005).

[88] F. Cunha et al., Langmuir **12**, 6410 (1996).

[89] D. Mayer, T. Dretschkow, K. Ataka, and T. Wandlowski, J. Electroanal. Chem. **524-525**, 20 (2002).

[90] X. Xiao, B. Xu, and N. J. Tao, Nano Letters **4**, 267 (2004).

[91] X. Li et al., J. Am. Chem. Soc. **128**, 2135 (2006).

[92] W. Haiss et al., Phys. Chem. Chem. Phys. **6**, 4330 (2004).

[93] M. Suzuki, S. Fujii, and M. Fujihira, Japanese J. of Appl. Phys. **45**, 2041 (2006).

[94] J. Ulrich, D. E. amd W. Pontius, L. Venkataraman, D. Millar, and L. H. Doerrer, J. Phys. Chem. B **110**, 2462 (2006).

[95] L. Venkataraman, J. E. Klare, I. W. T. amd C. Nuckolls, M. S. Hybertsen, and M. L. Steigerwald, Nano Letters **6**, 458 (2006).

[96] A. M. Rawlett et al., Appl. Phys. Lett. **81**, 3043 (2002).

[97] A. S. Blum, J. C. Yang, R. Shashidhar, and B. Ratna, Appl. Phys. Lett. **82**, 3322 (2003).

[98] D. S. Seferos, A. S. Blum, J. G. Kushmerick, and G. C. Bazan, J. Am. Chem. Soc. **128**, 11260 (2006).

[99] J. G. Kushmerick et al., J. Am. Chem. Soc **124**, 10654 (2002).

[100] D. S. Seferos, S. A. Trammell, G. C. Bazan, and J. G. Kushmerick, PNAS **102**, 8821 (2005).

[101] L. T. Cai et al., J. Phys. Chem B **108**, 2827 (2004).

[102] T. Hassenkam et al., Nano Letters **4 (1)**, 19 (2004).

[103] J. Chen et al., Appl. Phys. Lett. **77**, 1224 (2000).

[104] J. Liao, L. Bernard, M. Langer, C. Schönenberger, and M. Calame, Advanced Materials **18**, 2444 (2006).

[105] M. Mayor et al., Angew. Chem. Int. Ed. **42**, 5834 (2003).

[106] W. Haiss et al., Nature Materials **5**, 995 (2006).

[107] L. Venkataraman, J. E. Klare, C. Nuckolls, M. S. Hybertsen, and M. L. Steigerwald, Nature **442**, 904 (2006).

[108] J. Tomfohr and O. F. Sankey, J. Chem. Phys **120**, 1542 (2004).

[109] M. Paulsson, T. Frederiksen, and M. Brandbyge, Nano Letters **6**, 258 (2006).

[110] P. V. James, P. K. Sudeep, C. H. Suresh, and K. G. Thomas, J. Phys. Chem. A **110**, 4329 (2006).

[111] R. M. Metzger, Acc. Chem. Res. 1999, 32, 950-957 **32**, 950 (1999).

[112] R. M. Metzger, J. of Solid State Chem. **168**, 696 (2002).

[113] Y. Luo et al., ChemPhysChem **3**, 519 (2002).

[114] J. K. Sørensen et al., Org. Lett. **8**, 1173 (2006).

[115] X. Li et al., Faraday Discuss. **131**, 111 (2006).

[116] B. Q. Xu, X. L. Li, X. Y. Xiao, H. Sakaguchi, and N. J. Tao, Nano Letters **5**, 1491 (2005).

[117] X. Xiao, B. Xu, and N. Tao, Angew. Chem. Int. Ed. **43**, 6148 (2004).

[118] W. R. Browne and B. L. Feringa, Nature Nanotechnology **1**, 25 (2006).

[119] N. Weibel, S. Grunder, and M. Mayor, Org. Biomol. Chem. **5**, 2343 (2007).

[120] B. L. Feringa, J. Org. Chem. **72**, 6635 (2007).

[121] S. Grunder et al., J. Org. Chem. **72**, 8337 (2007).

[122] K. W. Hipps, Science **294**, 536 (2001).

[123] F. Chen, X. Li, J. Hihath, Z. Huang, and N. Tao, JACS **128**, 15874 (2006).

[124] R. Huber, Palladium break junctions, Master's thesis, University Basel, 2003.

Appendix A

Autoranging low-noise current to voltage converter

In this part of the appendix I would like to describe in more detail the Autoranging Low-Noise Current to Voltage Converter (AIVC) which was developed by Michael Steinacher.

The block diagram of the AIVC with the spike-killer is given in Fig. A.1. To ensure low-noise performance the AIVC is subdivide into two separated well shielded aluminum boxes (dashed lines): The first box holds the I to V Converter with the electronic gain switch and the digital optical isolation, realized by a dual optocoupler (ILD2, Vishay Semiconductors). The I to V converter box is designed to work also with other gain-control devices (e.g. direct from a PC); so the optical isolation prevents from noise coupling to the feedback resistor trough the gain switch. Furthermore it eliminates unwanted ground loops via the external gain-control device (PC).

A low-noise, precision and high-speed operational amplifier (OP) with J-FET input stage is used in I to V Converter stage (OPA627BP, Burr-Brown / Texas Instruments). It has a typical input voltage noise density of $8 \text{ nV}/\sqrt{Hz}$ and input current noise density of $1.6 \text{ fA}/\sqrt{Hz}$, both specified at a frequency of 100 Hz. That's why, for high impedance sources, the most noise is generated by the thermal noise of the feedback resistor, which is at room temperature: In the lowest range (105 V/A) the 100 kΩ feedback resistor has a thermal noise density of $41 \text{ nV}/\sqrt{Hz}$ which is a factor of five times higher than the voltage noise of the OP; it corresponds to an current noise density of $410 \text{ fA}/\sqrt{Hz}$. In the highest range (108 V/A) the 100 MΩ feedback resistor contributes a thermal noise density of $1.3 \text{ } \mu V/\sqrt{(Hz)}$ which
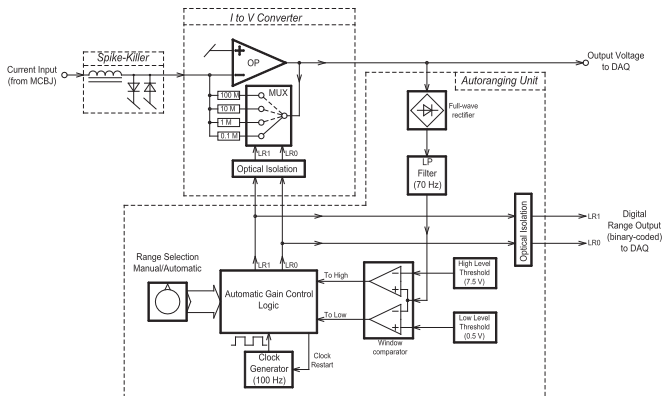
Figure A.1: The AIVC is partition into three shielded boxes, shown by dashed lines. The passive spike-killer suppresses the glitches from the I to V converter during gain switching. For low-noise performance the digital lines are isolated by optocouplers. The autoranging unit is a simple and robust circuit and it works for bipolar and AC signals. The converter as well as the autoranging unit is supplied by the same $\pm 15V$ low-noise power supply.

is equal to an current noise density of 13 fA$\sqrt{Hz}$; this is a factor of eight higher than the specified input current noise density of the OP. With the input of the AIVC left open, the measured current noise density in the 108 V/A range is given in Fig. A.2; the noise floor is around 15 fA/$\sqrt{Hz}$. The peaks at 50 Hz and 100 Hz are coming from the 50 Hz line voltage and its harmonics. At such low levels the stray pick-up of line harmonic-frequencies is almost inevitable. Concerning the 800 Hz signal bandwidth of the highest range (108 V/A), the total noise is $\sim$ 0.5 pA$_{rms}$. The maximum output voltage swing of the I to V converter is $\pm$ 12 V; it is designed to drive high impedance loads larger than 10 kΩ. For selecting one of the four different feedback resistors (accuracy ± 1 %), a 4-channel CMOS analog multiplexer (MUX) is used (DG409, Intersil). It has a typical ON resistance of 40 Ω, an OFF capacitance of 3 pF and a switching time of 250 ns. With these components a bandwidth (-3 dB) of around 800 Hz can be reached for the highest range of 108 V/A. For the other ranges (107, 106, 105 V/A) the bandwidth is restricted to around 10 kHz by capacitors in parallel with the feedback resistors. The charge injection during the switching operation of this electronic multiplexer is typical 20 pC. This parasitic charge injection,
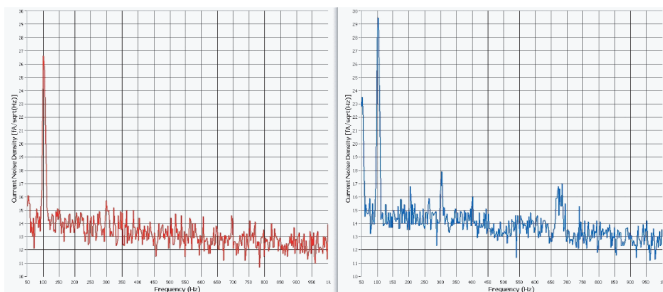
Figure A.2: The graph on the left (red) shows the current noise density of the AIVC at a gain of 108 V/A while the input is left open and no spike-killer is attached. On the right graph (blue) the same measurement is repeated but the spike-killer, equipped with two low leakage silicon diodes (BAS45A), is attached to the input of the AIVC. The noise floor is only slightly raised by the spike-killer. The 50 Hz line frequency and some of its harmonics can be identified on the graphs. Both graphs show a frequency span from 50 Hz to 1 kHz and the x-axis corresponds to the current noise density converted from the measured voltage noise density. The measurements are achieved with a HP3589A spectrum analyzer by averaging 100 sweeps.

in combination with the limited impulse response of the OP, generates the spikes at the input of the I to V converter. On high impedance sources these spikes, during the range switching, can reach levels of several volts. But the spikes are very short in time (in the μs range) which corresponds to high frequencies. Electrostatic sensitive samples need a spike-killer between the sample and the input of the AIVC. It reduces the glitches by typical two orders of magnitude which is then no longer a problem, also for very sensitive samples. The SK contains two anti-parallel diodes wired to ground and a large inductance (120 mH) between the input of the AIVC and the sample. Three different types of inductors are interconnected in series, resulting in a broadband frequency response. In combination with the capacitances of the connection cable and the sample, this inductance forms an efficient low-pass filter for the fast spikes. The anti-parallel diodes restrict the glitch-levels at the input to maximum $\pm$ 0.7 V if silicon diodes (BAS45A) are used; respective to maximum $\pm$ 0.3 V with Schottky diodes (BAT81). Schottky diodes reduce the spike level more efficient but they highly increase the noise level of the converter due to their high leakage current. When low leakage silicon diodes (BAS45A) are installed, the noise level of the I to V converter is only slightly raised by the SK (see Fig. A.2).
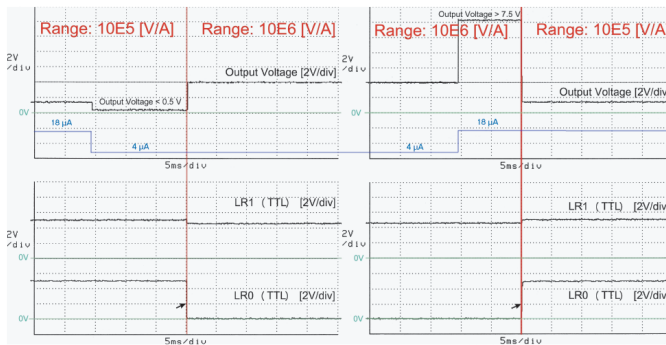
Figure A.3: The left diagram shows the signal response of an upward range switch from 105 V/A to 106 V/A. It is triggered due to a drop in the output voltage from 1.8 V to 0.4 V which corresponds to a drop in input current from 18 μA to 4 μA. After around 15 ms the next higher range is selected and the output voltage reaches 4 V, corresponding to 4 μA. The right chart shows the signals for a downward range adjustment from 106 V/A to 105 V/A where the 4 μA input current (corresponding to the 4 V output voltage) jumps again back to 18 μA. This input current drives the convert to its maximum output voltage of around 12 V. After about 10 ms the next lower range is chosen and the measured voltage is valid again. In both diagrams the top line (black) shows the measured output voltage of the AVIC; underneath the input current is drawn (blue) for clarity. The bottom two lines (black) show the binary coded linear range signals (LR1, LR0). Both diagrams have a horizontal grid of 5 ms per division.

In the second well shielded box, the auto ranging unit is installed. The output voltage of the converter is full-wave rectified by an active circuit without any diode voltage drop. This full-wave processing is needed for the bipolar and AC function of the auto ranging unit. A 70 Hz low pass (LP) filter provides the arithmetic mean value of the rectified signal. The LP filter prevents the electronics from false triggering on short pulses on the output voltage. A window comparator detects whether the mean value is smaller than 0.5 V (Low Level Threshold) or higher than 7.5 V (High Level Threshold). The corresponding signals generated by the window comparator are named 'To Low' and 'To High'. If one of these signals is true, the 100 Hz clock generator (LMC555, National Semiconductors) is restarted (Clock Restart) and it runs for around 100 ms. This synchronization of the clock generator with the signal 'To High' or 'To Low' makes sure, that the range switching takes always the same time of around 10 to 15 ms. Due to the time response of the first order 70 Hz LP-filter, the exact switching time de-

pends on the shape and amplitude of the signal. The clock-synchronization ensures that a range switch is carried out only, if an over- or underflow is detected during a minimum period of 10 ms; this leads to a very robust auto ranging behavior. The left diagram of Fig. A.3 shows the signals during an underflow (output voltage < 0.5 V) which initiates the range switches from 105 V/A to 106 V/A. The range switch in opposite direction is shown on the right diagram; it is triggered by an overflow (output voltage > 7.5 V). The largest range switch from the 108 V/A to the 105 V/A range (and vice versa) takes three steps and needs a time of around 35 ms. If a sinusoidal AC signal (frequency 300...600 Hz) is used, the AC switching levels correspond to $0.56 V_{rms}$ (To Low) and $8.33 V_{rms}$ (To High). The automatic gain control (AGC) logic switches to the next higher range when the signal 'To Low' is activated; analogous the next lower range is chosen when the signal 'To High' is active. If the highest range of 108 V/A is already reached and the signal 'To Low' is activated, the device remains at the actual range. The same happens in the lowest range of 105 V/A if the signal 'To High' is true. The range can also be selected manually by a rotary switch (Range Selection Manual/Automatic); then the AGC function is disabled. The AGC-logic is based on a two bit up/down counter clocked by falling edge of the external 100 Hz generator; it is realized with a programmable logic chip (GAL16V8, Lattice). The selected range is binary coded in the two signals LR1, LR0. The digital (TTL) range signals are sent to the I to V converter as well as to the DAQ via an optical isolation (optocoupler ILD2, Vishay Semiconductors). Parasitic ground loops from the digital part of the DAQ can be prevented by this optical isolation.

The complete electronics is supplied by a low-noise linear $\pm$ 15 V power supply; the power consumption of the AIVC is around 1.2 W.
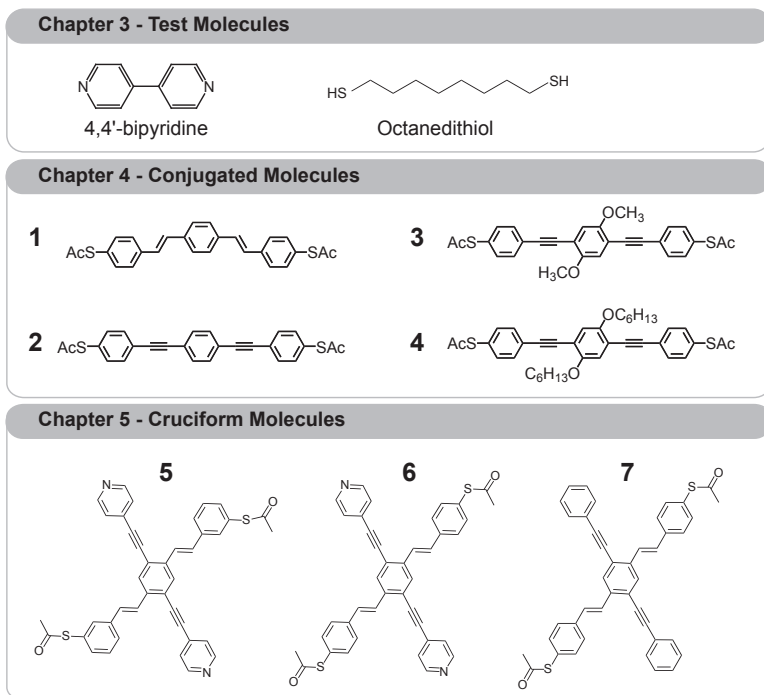
Appendix B

Molecules overview

Institutes

CUB	Department of Chemistry, University of Basel,Switzerland	Prof. M. Mayor Dr. M. Langer
FZK	Forschungszentrum Karlsruhe GmbH, Institute for Nanotechnology, Germany	Prof. M. Mayor
CUD	Department of Chemistry, University of Durham, UK	Prof. M. Bryce

Figure B.1: Overview on the molecules which were investigated in this thesis.

Transformation between the log- and linear histograms

Here we derive the transformation between the *logarithmic* and *linear* histogram, which we have used before for the presentation of the measured electrical conductance values G.

Histograms are constructed from a set of measured conductance values $G_{j,i}^{><} = G_j^{><}(z_i)$, acquired repetitively (index j) during opening ($>$) and closing ($<$) of the junctions. z_i denotes the push-rod position at the instance of a measurement, acquired and stored in the computer. Because we only focus on the dependence of G while opening the junction in this work, we disregard $G^<$ in the following. Furthermore, we will also assume that the successive z-values, i.e. z_i, z_{i+1}, are lying so dense that a continuum approximation is justified. We introduce the abbreviation $g = log(G)$ and N_{tot} for the total number of points entering both the G and $logG$-histogram.

Let $p_G(G)$ denote the probability to measure a conductance value in the interval $G \ldots G+dG$, and similarly $p_g(g)$ the probability to measure a g-value in the interval $g \ldots g + dg$. Then, the relation

$$p_G(G)dG = p_g(g)dg \qquad (C.1)$$

holds. Because $g = log(G)$, it further follows that

$$dg = d(logG) = log(e)d(lnG) = log(e)\frac{dG}{G} \, . \qquad (C.2)$$

Taking eq C.1 and eq C.2, yields the relation

$$p_G = p_g log(e)/G \,. \tag{C.3}$$

If we denote with ΔG and Δg the respective bin-widths of the linear and log-histogram, the linear $N_G(G)$ and the log-histogram $N_g(g)$ are defined by:

$$N_G(G) = N_{tot}p_G(G)\Delta G \tag{C.4}$$

$$N_g(g) = N_{tot}p_g(g)\Delta g \,. \tag{C.5}$$

Replacing p_G in eq C.4 with eq C.3 and combining with eq C.5, yields the final result:

$$N_G(G) = N_g(logG)\frac{log(e)}{G}\frac{\Delta G}{\Delta g} \,. \tag{C.6}$$

This equation shows that if the log-histogram $N_g(g)$ is constant, the linear histogram $N_G(G)$ is proportional $1/G$, as shown in Section 3.2.

Appendix D

Influence of the background subtraction on the conductance value

As described in Chapter 3 the tunneling background in the linear histogram is proportional to $1/G$ while it is constant in the log-scale histograms. In this short Section we would like to show that subtracting the background does influence the conductance value only very little. As an example we use the OPV measurement also shown in Fig. 4.2 and 4.4(a). We choose two different backgrounds in Fig. D.1(a) whereas background 1 is clearly too high and background 2 is far too low. The intermediate background 2 is usually used to analyze the data. Fig. D.1(b) now shows the data after the subtraction of the background. The gaussian dashed lines highlight the peaks and the two arrows point to the maximum values. The conductance value of this two peaks changes only marginal. If we subtract too few we obtain $2.1 \cdot 10^{-4} G_0$ which is similar to the value shown in tab. 4.2. When subtracting too much the peak shifts slightly to the right and gives $2.3 \cdot 10^{-4} G_0$. Therefore, with the proper selection of the background this should not be an issue.
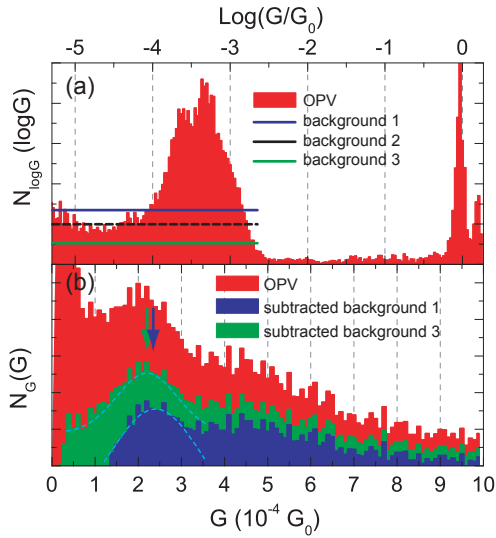
Figure D.1: Measurement of OPV. The graph shows the only small influence of the background subtraction on the graph in linear scale.

Additional data of OPE measurements

In Chapter 4 we have shown the sample to sample variance of 3 OPV measurements. Now, in this Appendix the data of 3 different samples of OPE (molecule **2**) measurements are shown. The histograms are built of 100 curves. Fig. E.1 presents the sample to sample variation in the Log histograms, whereas Fig. E.2 shows the same data in linear scale. The histograms of measurements with sidegroup-OPEs (**3** and **4**) look similar.
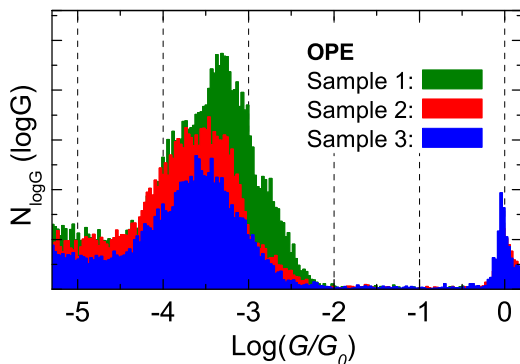
Figure E.1: OPE Log-histograms of 3 different samples and measurements.
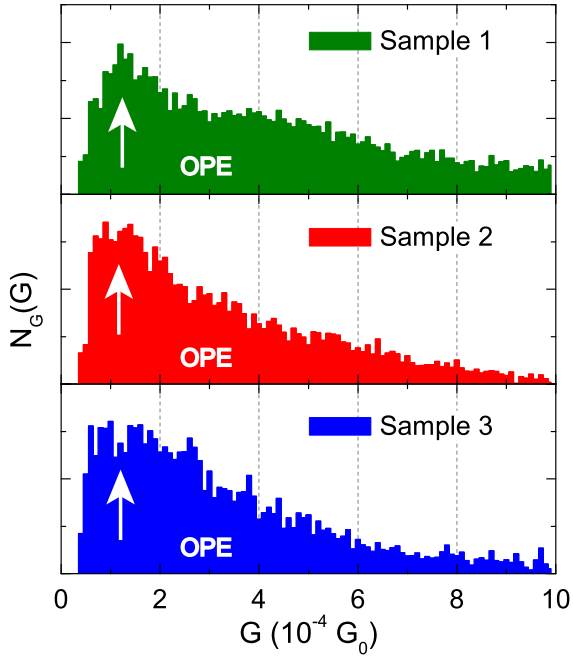
Figure E.2: Linear histograms of the same three samples as shown in Fig. E.1. All three histograms have the maximum at a conductance value of $\sim 1.1 \cdot 10^{-4} G_0$.

The polyimide covered break junction sample

In the following we show single conductance curves during opening a break junction in different solvents, compared to a polyimide covered junction. The single curves reach a saturation point, due to the offset current of the AIVC ($2 \cdot 10^{-7}G_0$) and the leakage current.

The blue curves show the saturation in a mixture of THF/mesitylene. The deduced leakage current is low at $\sim 8 \cdot 10^- 7G_0$. When immersing the sample in ethanol, the leakage current increases by more than an order of magnitude (violet curve). When covering the junction with polyimide, the leakage current is reduced again by $\sim$ a factor of 5 (red curves).
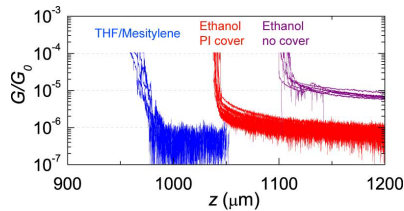
Figure F.1: Saturation point in different solvents compared to a polyimide covered junction.

Figure F.2: An example of a polyimide clotted sample. Colored for the NCCR picture contest.

Figure F.3: An example of a polyimide clotted sample. Colored for the NCCR picture contest.

Publication List

Articles

- *Electrical conductance of atomic contacts in liquid environments.*
  L. Grüter, M.T. González, R. Huber, M. Calame and C. Schönenberger, Small **1**, 1067, (2005).

- *Electrical Conductance of Molecular Junctions by a Robust Statistical Analysis.*
  M. T. González, S. Wu, R. Huber, S. J. van der Molen, C. Schönenberger and M. Calame, Nano Letters **6**, 2238 (2006).

- *Feedback controlled electromigration in four-terminal nano-junctions.*
  Z. M. Wu, M. Steinacher, R. Huber, M. Calame, S. J. van der Molen and C. Schönenberger, Appl. Phys. Lett. **91**, 053118 (2007).

- *New Cruciform Structures: Toward Coordination Induced Single Molecule Switches.*
  S. Grunder, R. Huber, V. Horhoiu, M. T. González, C. Schönenberger, M. Calame and M. Mayor, J. Org. Chem. **72**, 8337 (2007).

- *Electrical conductance of conjugated oligomers at the single molecule level*
  R. Huber, M. T. González, S. Wu, M. Langer, S. Grunder, V. Horhoiu, M. Mayor, M. Bryce, C. Wang, R. Jitchati, C. Schönenberger, and M. Calame, JACS **130**, 1080 (2008).

- *Conductance values of alkanedithiol molecular junctions.* M. T. González, J. Brunner, R. Huber, S. Wu, C. Schönenberger, and M. Calame, submitted to New Journal of Physics.

- *Aromatic Coupling Induced Single Molecular Junctions.* S. Wu, R. Huber, M. T. González, S. Grunder, M. Mayor, C. Schönenberger, and M. Calame, submitted to Nature Nanotech.

- *Autoranging Low-Noise Current to Voltage Converter.* M. Steinacher, C. Schönenberger, M. T. González, R. Huber, S. Wu and M. Calame, to be published.

Poster contributions

- *Break Junctions in liquid for molecular electronics.*
  R. Huber, Z. M. Wu, M. T. González, H. Breitenstein, P. Reimann, M. Calame and C. Schönenberger.
  Poster at the NCCR Nano meeting, Gwatt, October 6th - 7th, 2005

- *Break Junctions in liquid for molecular electronics.*
  R. Huber, S. Wu, M. T. González, H. Breitenstein, P. Reimann, C. Schönenberger and M. Calame.
  Poster at the International Workshop on Molecular Electronics, Řež (near Prague), Czech Republic, June 30th - July 4th, 2006.

- *Statistical Study of Single-Molecular-Junctions Conductance.*
  R. Huber, S. Wu, M. T. González, S. J. van der Molen, H. Breitenstein, P. Reimann, M. Steinacher, V. Horhoiu, S. Grunder, M. Mayor, C. Schönenberger and M. Calame.
  Poster at the NCCR Nano meeting, Basel, April 25th, 2007.

Talks

- *Break Junctions in liquid for molecular electronics.*
  Talk at the NCCR Nano meeting, Basel, April 12th 2006.

- *Break Junctions in liquid for molecular electronics.*
  Talk at the NCCR Nano meeting, PSI Villigen, November 15th 2006

- *Break Junctions in liquid for molecular electronics.*
  Talk at the annual meeting of the Swiss Physical Society, Zürich, February 12th 2007.

- *From simple conjugated molecules to coordination induced single molecule switches*
  Talk at the annual meeting of the Swiss Physical Society, Geneva, March 26th, 2008.

Currriculum Vitae

Roman A. Huber

- 23.9.1978
  Geboren in Basel, Schweiz

- 1985-1994
  Besuch der Primar- und Sekundarschule Liestal

- 1994-1997
  Besuch des Gymnasium Liestal

- 1998-2003
  Physikstudium an der Universität Basel

- 2002-2003
  Stellvertretende Lehrkraft an der Sekundarschule Liestal

- 2003
  Diplomarbeit zum Thema: "Palladium Breakjunctions" bei Prof. C. Schönenberger

- 2003
  Diplom in Physik

- Februar 2004
  Beginn der vorliegenden Dissertation

- Januar 2008
  Erfolgreicher Abschluss der vorliegenden Dissertation

- 2004-2007
  Assistenz zu den Vorlesungen "Physik I und II"

Folgenden Dozentinnen und Dozenten verdanke ich meine Ausbildung:
C. Bandle, R. Bennewitz, C. Bruder, H. Burkhart, A. Bussmann-Holder,
H.-J. Hug, D. Masser, E. Meyer, H.-J. Güntherodt, M. Hegner, M. Calame,
G.-R. Plattner, I. Sick, C.Schönenberger, L. Tauscher, F.-K. Thielemann,
D. Trautmann.

Acknowledgements